RESEARCH ARTICLE

A Molecular Switch between Mammalian MLL Complexes Dictates Response to Menin–MLL Inhibition

Yadira M. Soto-Feliciano[1], Francisco J. Sánchez-Rivera[2], Florian Perner[3,4,5], Douglas W. Barrows[1,6], Edward R. Kastenhuber[2], Yu-Jui Ho[2], Thomas Carroll[6], Yijun Xiong[3,4], Disha Anand[3,5], Alexey A. Soshnev[1], Leah Gates[1], Mary Clare Beytagh[1], David Cheon[1], Shengqing Gu[7,8], X. Shirley Liu[7,8], Andrei V. Krivtsov[3,4], Maximiliano Meneses[9], Elisa de Stanchina[9], Richard M. Stone[10], Scott A. Armstrong[3,4], Scott W. Lowe[2], and C. David Allis[1]

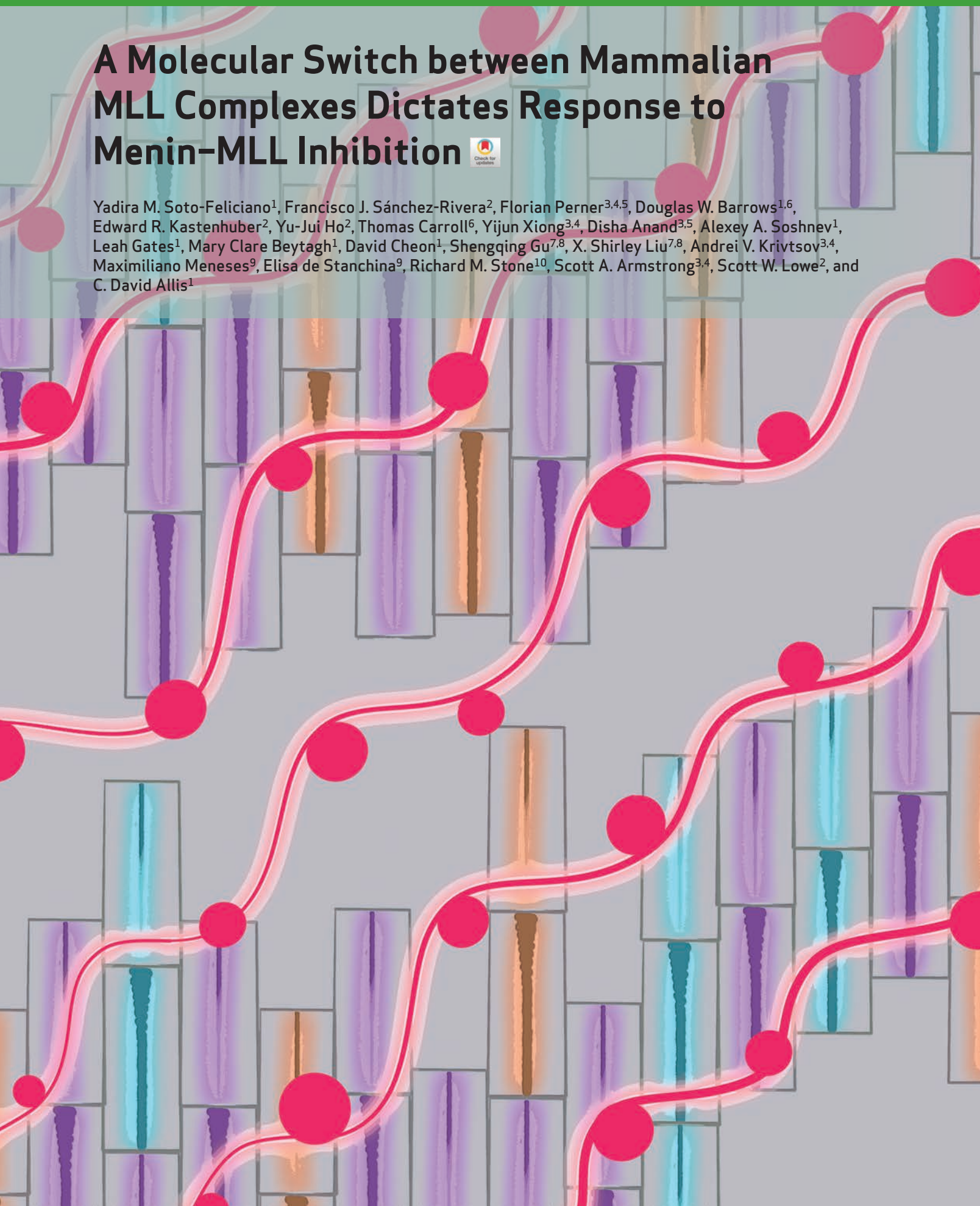

ABSTRACT Menin interacts with oncogenic MLL1-fusion proteins, and small molecules that disrupt these associations are in clinical trials for leukemia treatment. By integrating chromatin-focused and genome-wide CRISPR screens with genetic, pharmacologic, and biochemical approaches, we discovered a conserved molecular switch between the MLL1–Menin and MLL3/4–UTX chromatin-modifying complexes that dictates response to Menin–MLL inhibitors. MLL1–Menin safeguards leukemia survival by impeding the binding of the MLL3/4–UTX complex at a subset of target gene promoters. Disrupting the Menin–MLL1 interaction triggers UTX-dependent transcriptional activation of a tumor-suppressive program that dictates therapeutic responses in murine and human leukemia. Therapeutic reactivation of this program using CDK4/6 inhibitors mitigates treatment resistance in leukemia cells that are insensitive to Menin inhibitors. These findings shed light on novel functions of evolutionarily conserved epigenetic mediators like MLL1–Menin and MLL3/4–UTX and are relevant to understand and target molecular pathways determining therapeutic responses in ongoing clinical trials.

SIGNIFICANCE: Menin–MLL inhibitors silence a canonical *HOX*- and *MEIS1*-dependent oncogenic gene expression program in leukemia. We discovered a parallel, noncanonical transcriptional program involving tumor suppressor genes that are repressed in Menin–MLL inhibitor–resistant leukemia cells but that can be reactivated upon combinatorial treatment with CDK4/6 inhibitors to augment therapy responses.

INTRODUCTION

Menin is an evolutionarily conserved nuclear factor that associates with chromatin to recruit (adapt) interacting proteins (1). These include the Trithorax (Trx)-related MLL1 (KMT2A) and MLL2 (KMT2B) histone methyltransferase complexes (2, 3), MLL1 oncogenic fusion proteins (4), transcription factors [e.g., c-MYC (5), JUND (6, 7), SMADs (8, 9)], and other chromatin-bound proteins [e.g., LEDGF (10); reviewed in ref. 11].

Menin is a core subunit of the MLL1 (ref. 12) and MLL2 complexes (2) and is responsible for targeting these to chromatin (3). Menin is required for MLL1/MLL2-dependent H3K4 trimethylation of *HOX* genes and their stable long-term expression during development (2, 13). Menin has context-specific functions in human diseases, acting as a tumor suppressor in neuroendocrine malignancies (14, 15) and in certain skin (16), lung (17), and central nervous system (CNS) tumors (18) and as an oncogenic cofactor in other cancers, including hepatocellular carcinoma (19) and *MLL1*-rearranged (*MLL1*-r) leukemias (4, 20). Furthermore, over 1,000 germline and somatic *MEN1* variants have been identified, some of which are linked to cancer predisposition (21).

Given the pro-oncogenic role of Menin in acute leukemia and other malignancies, small-molecule inhibitors targeting the Menin–MLL1 and Menin–MLL2 protein–protein interactions have shown great promise for intercepting and treating different types of cancers (19, 22–27). Notably, three structurally different Menin–MLL inhibitors have recently entered clinical trials (NCT04065399, NCT04067336, and NCT04811560), and at least one has been granted fast-track designation by the FDA for the treatment of relapsed/refractory acute leukemias (25, 27, 28). Thus, an understanding of the molecular mechanisms of action of these drugs would facilitate the development of biomarkers to predict therapeutic response and resistance, and lead to the rational design of more effective combination treatments.

[1]Laboratory of Chromatin Biology and Epigenetics, The Rockefeller University, New York, New York. [2]Cancer Biology and Genetics, Memorial Sloan Kettering Cancer Center, New York, New York. [3]Department of Pediatric Oncology, Dana-Farber Cancer Institute, Boston, Massachusetts. [4]Division of Hematology/Oncology, Boston Children's Hospital and Harvard Medical School, Boston, Massachusetts. [5]Internal Medicine C, Greifswald University Medical Center, Greifswald, Germany. [6]Bioinformatics Resource Center, The Rockefeller University, New York, New York. [7]Department of Biostatistics and Computational Biology, Dana-Farber Cancer Institute, Harvard School of Public Health, Boston, Massachusetts. [8]Center for Functional Cancer Epigenetics, Dana-Farber Cancer Institute, Boston, Massachusetts. [9]Antitumor Assessment Core Facility, Memorial Sloan Kettering Cancer Center, New York, New York. [10]Leukemia Division, Department of Medical Oncology, Dana-Farber Cancer Institute, Boston, Massachusetts.

Current address for Y.M. Soto-Feliciano and F.J. Sánchez-Rivera: David H. Koch Institute for Integrative Cancer Research and Department of Biology, Massachusetts Institute of Technology, Cambridge, Massachusetts.

Y.M. Soto-Feliciano, F.J. Sánchez-Rivera, and F. Perner are co–first authors.

Corresponding Authors: C. David Allis, The Rockefeller University, Allis Lab, Box #78, 1230 York Avenue, New York, NY 10065. Phone: 212-327-7839; E-mail: alliscd@rockefeller.edu; Scott W. Lowe, Memorial Sloan Kettering Cancer Center, Sloan Kettering Institute, Cancer Biology and Genetics Program, New York, NY, 10065. Phone: 646-888-3342; E-mail: lowes@mskcc.org; and Scott A. Armstrong, Harvard Medical School, Dana-Farber Cancer Institute, Department of Pediatric Oncology, Boston, MA, 02115. Phone: 617-632-2991; E-mail: Scott_Armstrong@dfci.harvard.edu

Cancer Discov 2023;13:146–69

doi: 10.1158/2159-8290.CD-22-0416

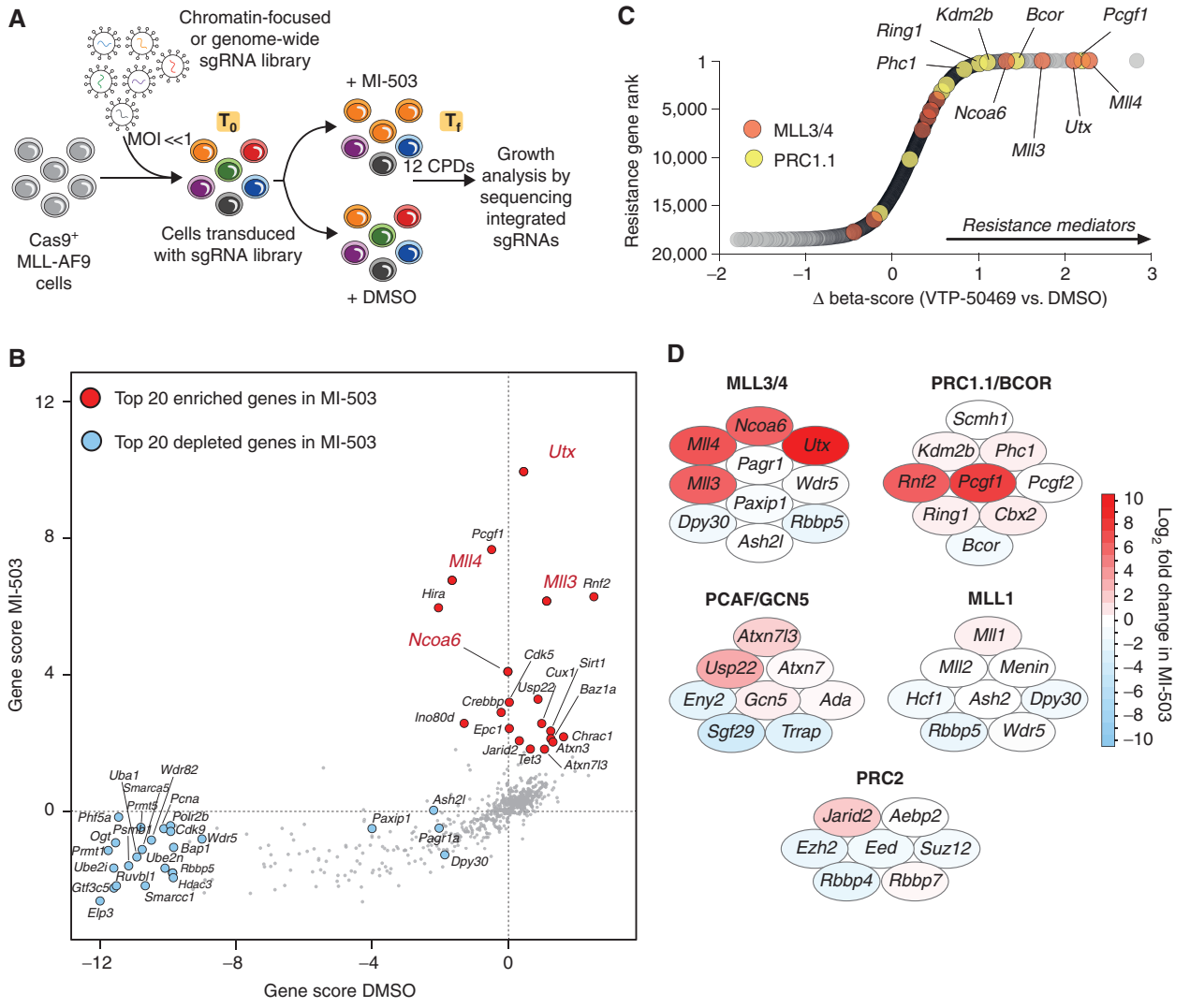

Figure 1. CRISPR screens uncover the functional interplay between the mammalian MLL1 and MLL3/4 chromatin-modifying complexes. **A,** CRISPR-Cas9-based screening strategy to identify regulators of response to Menin–MLL inhibition. CPD, cell population doublings; sgRNA, single-guide RNA; T_f, final time point; T_0, initial time point. **B,** Chromatin-focused CRISPR screening data showing the top 20 most significantly enriched (red) and depleted (blue) genes in the Menin–MLL inhibitor (MI-503) treatment relative to vehicle (DMSO). Gene scores are shown as the mean $\log_2$ fold change in abundance of the 6 sgRNAs targeting each gene in each condition. **C,** Genome-wide CRISPR screening data showing gene-level ranking based on differential enrichment of sgRNAs in the Menin–MLL inhibitor treatment (VTP-50469) relative to vehicle (DMSO). Differential (Δ) beta-score between VTP-50469 and DMSO conditions was calculated using MaGeCK. A positive Δ beta-score denotes enrichment of specific gene-targeting sgRNAs. A negative Δ beta-score denotes depletion of specific gene-targeting sgRNAs. Red circles denote MLL3/4–UTX complex subunits. Yellow circles denote PRC1.1 complex subunits. **D,** Schematic representation of the top-scoring chromatin regulators in the chromatin-focused MI-503 screen and their corresponding protein complexes. Red denotes enriched subunits. Blue denotes depleted subunits. Color scale represents the $\log_2$ fold change in abundance of the 6 sgRNAs targeting each subunit in the Menin–MLL inhibitor (MI-503) treatment relative to vehicle (DMSO). (*continued on following page*)

RESULTS

Functional Interplay between MLL1–Menin and MLL3/4–UTX Chromatin-Modifying Complexes

To understand the dependency of *MLL1*-r leukemias to Menin and identify factors that dictate response and resistance to Menin–MLL inhibitors, we performed a series of CRISPR-based genetic screens. First, we screened a chromatin-focused CRISPR library in Cas9-expressing mouse leukemia cells driven by a human *MLL1–AF9* transgene (hereafter referred to as MLL-AF9 cells; ref. 29; Supplementary Fig. S1A–S1G; Supplementary Table S1). Library-transduced cells were cultured in media with DMSO (vehicle) or a Menin–MLL inhibitor (MI-503; ref. 22) for 12 cell population doublings, followed by screen deconvolution using next-generation sequencing (Fig. 1A). We calculated a score for each gene included in the library by assessing the changes in abundance of single-guide RNAs (sgRNA) during the culture period (Fig. 1B). Consistent with previous work, sgRNAs targeting known *MLL1*-r leukemia dependencies, including *Dot1L* (29–32), *Brd4* (33), and *Myb* (34), were strongly depleted in both treatments, whereas control sgRNAs remained largely neutral (Supplementary Table S2).

We observed that sgRNAs targeting the histone H3 lysine 27 (H3K27) demethylase *Utx* (*Kdm6a*) and the histone H3

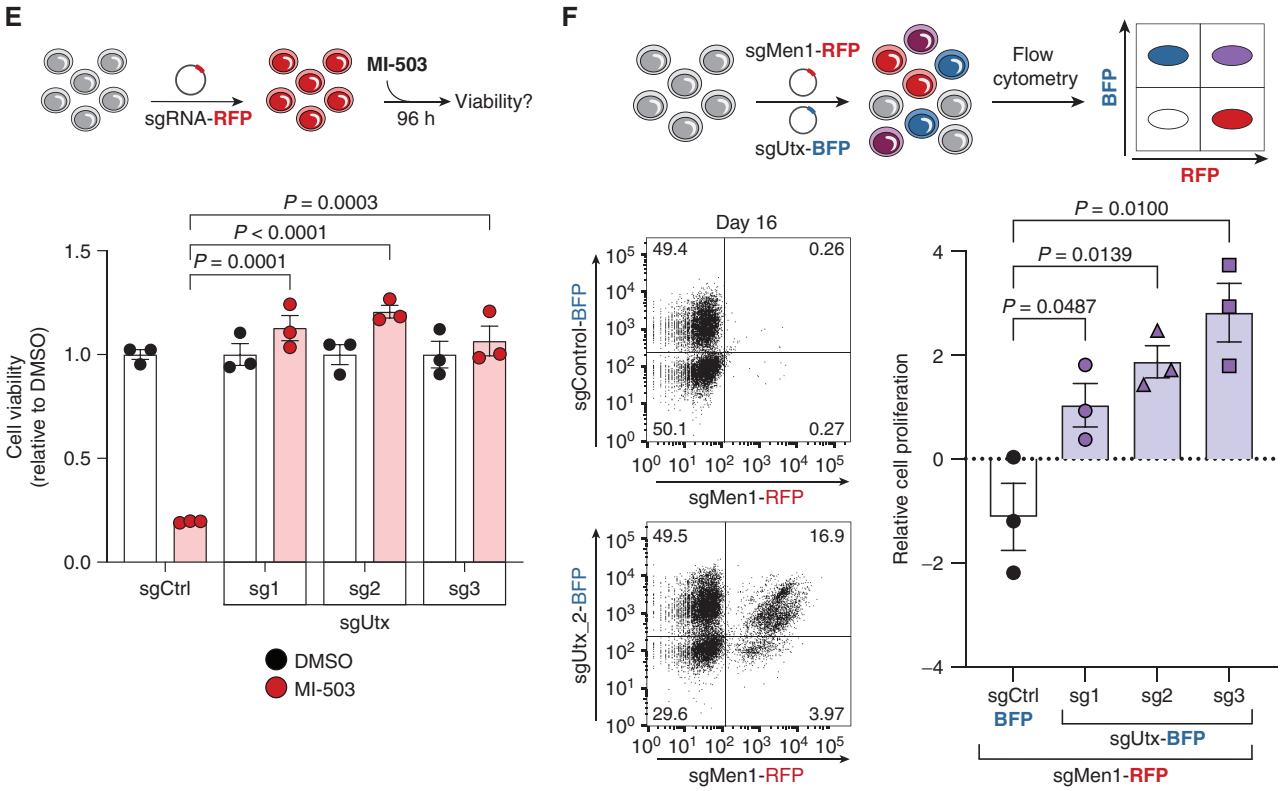

Figure 1. ***(Continued)*** **E,** Viability assay from cells treated with vehicle (DMSO, black) or Menin–MLL inhibitor (MI-503, red) for 96 hours (mean ± SEM, $n = 3$ infection replicates, P values calculated by Student t test). sgCtrl, control sgRNA targeting a nongenic region on chromosome 8. **F,** Relative cell proliferation is shown as the proliferation of double-positive cells (sgMen1-RFP + sgUtx-BFP or sgMen1-RFP + sgCtrl-BFP) relative to single-positive cells (sgMen1-RFP) 16 days after infection measured by flow cytometry (mean ± SEM, $n = 3$ infection replicates, P values calculated by Student t test). Representative FACS plots are shown for sgControl- and sgUtx-targeted cells.

lysine 4 (H3K4) monomethyltransferases *Mll3* (*Kmt2c*) and *Mll4* (*Kmt2d*) were the most significantly enriched in the Menin–MLL inhibitor context (Fig. 1B, red circles). This result was unexpected given previously described canonical functions for the mammalian MLL complexes (35). For example, the MLL1/2–Menin complex (disrupted by MI-503) is known to catalyze chromatin modifications associated with transcription at promoters, including dimethylation or trimethylation of H3K4 (H3K4me2/3; refs. 13, 36, 37). On the other hand, the MLL3/4–UTX complex has been shown to regulate enhancer states by serving as the major H3K4 monomethyltransferase (H3K4me1; refs. 38–42).

To assess whether these results were idiosyncratic of the cell line, library, or inhibitor used, we performed a genome-wide CRISPR screen in an independently derived MLL-AF9 mouse cell line using VTP-50469, a more potent (than MI-503), selective, and orally bioavailable Menin–MLL inhibitor (25, 27, 28). sgRNAs targeting *Utx*, *Mll3*, and *Mll4* were also among the most significantly enriched candidate genes identified in this genome-wide screen (Fig. 1C; Supplementary Fig. S2A–S2C; Supplementary Table S2), whereas shared subunits between the two types of MLL complexes scored similarly in both vehicle and Menin–MLL inhibitor conditions (Fig. 1B–D; Supplementary Fig. S2D). These results suggest that the core subunits of the MLL3/4–UTX complex modulate the therapeutic response of leukemia cells to Menin–MLL inhibition, pointing to a previously unknown functional cross-talk between these chromatin-modifying complexes.

To determine the effects of MLL3/4–UTX loss of function in leukemia cell proliferation, we performed *in vitro* growth competition assays (Supplementary Fig. S3A). We found that *Utx* or *Mll3* inactivation by CRISPR did not have a significant impact on leukemia cell proliferation, but *Mll4* inactivation decreased leukemia cell growth (ref. 43; Supplementary Fig. S3B–S3D). Consistent with our genetic screening results, *Utx* inactivation using three distinct sgRNAs significantly increased the viability of MI-503–treated leukemia cells relative to their wild-type counterparts (Fig. 1E; Supplementary Fig. S3E). In addition, *Mll3*- or *Mll4*-deficient leukemia cells treated with MI-503 exhibited a proliferative advantage over wild-type cells under drug treatment (Supplementary Fig. S3F and S3G). These orthogonal results establish the MLL3/4–UTX complex as a central modulator of therapy response to Menin–MLL inhibition in acute leukemia.

Because UTX was the most significantly enriched chromatin factor in our screen and this protein is shared by both MLL3 and MLL4 complexes (42, 44, 45), we focused on UTX disruption to probe the molecular mechanisms linked to resistance to Menin–MLL inhibition. We first tested whether genetic *Utx* inactivation could rescue the effects of Menin-specific ablation in MLL-AF9 leukemia cells. CRISPR-mediated deletion of *Men1* led to robust inhibition of proliferation (Supplementary

Fig. S4A), but codeletion of *Utx* suppressed this phenotype, such that *Men1*-deficient MLL-AF9 cells were able to proliferate despite the presence of the drug (Fig. 1F; Supplementary Fig. S4B–S4F). These results establish a previously unknown epistatic relationship between *Men1* and *Utx* in acute leukemia. Of note, preexisting mutations in *MLL3*, *MLL4*, or *UTX*, some of which lead to truncated versions of the respective proteins, are found in about 8% of patients with acute myeloid leukemia (AML), myelodysplastic syndromes, or myeloproliferative neoplasia (Fig. 1F; Supplementary Fig. S4G). The experimental setup used for our experiments strived to model the consequent loss of function of MLL3/4–UTX proteins in these cases.

To determine if the genetic interaction between Menin and UTX depends on the MLL-fusion protein (MLL-FP), we ablated the *MLL1–AF9* oncogenic transgene used to generate this model using CRISPR-Cas9 (46–48). Importantly, survival of leukemia cells remains dependent on the presence of the MLL–AF9 fusion protein even when UTX is lost, demonstrating that MLL-FP–driven canonical gene expression is intact even after loss of MLL3/4 function (Supplementary Fig. S5A–S5C). Codeletion of *UTX* and *MEN1* in an *NPM1c*-mutant human leukemia cell line (49, 50) also bypassed the proliferation defects associated with loss of *MEN1* alone (Supplementary Fig. S5D and S5E). Therefore, Menin–MLL inhibitors act through an evolutionarily conserved pathway that involves a functional cross-talk between Menin and UTX and is downstream or independent of MLL-FPs.

Menin is required for expression of canonical MLL-FP target genes like *Meis1*, which is required for leukemia maintenance (25, 36, 37, 51, 52). Moreover, *Meis1* overexpression has been shown to partially rescue the leukemic stem cell transcriptional program suppressed by Menin–MLL inhibition (27). To determine if the genetic interaction between Menin and UTX regulates the expression of these MLL-FP targets, we first treated mouse MLL-AF9 leukemia cells with MI-503 and confirmed that it leads to the robust downregulation of *Meis1* (Supplementary Fig. S5F). However, to our surprise, cells genetically deficient for both *Men1* and *Utx* showed a similar reduction in *Meis1* levels (Supplementary Fig. S5G) yet were able to proliferate (Fig. 1F; Supplementary Fig. S4E). When we knocked out *Utx* in mouse leukemia cells, we observed that *Meis1* mRNA levels are not significantly different when compared with the Utx^{WT} counterparts (Supplementary Fig. S5H). We also observed significant downregulation of *Meis1* expression after treatment with a Menin–MLL inhibitor. These data support a genetic epistasis model between Menin and UTX in Menin-dependent mammalian cells and suggest that factors beyond *Meis1* can sustain the proliferative capacity of *MLL1*-r and non–*MLL1*-r leukemia cells.

The MLL1–Menin Complex Restricts Chromatin Occupancy of MLL3/4–UTX at Target Gene Promoters

Given previous work suggesting a primary role for Menin at promoters (6, 53) and UTX at enhancers (42), we performed chromatin immunoprecipitation followed by sequencing (ChIP-seq) to examine the genome-wide binding patterns of their respective protein complexes (Supplementary Table S3). As expected, Menin showed strong enrichment at promoter regions [here defined as transcription start sites (TSS) ± 2 kb], which was decreased when its canonical interactions with MLL1/2 and MLL-FPs were disrupted by MI-503 (Fig. 2A). Genome-wide enrichment of Menin was also decreased, as evidenced by the reduction in the number of ChIP peaks after MI-503 treatment (Supplementary Fig. S6A). We observed only a small number of UTX peaks under basal conditions; however, MI-503 treatment led to a substantial increase in UTX chromatin association, with predominant binding at promoters (Fig. 2B; Supplementary Fig. S6A). UTX binding sites detected after MI-503 treatment included those observed under basal conditions and more than 13,000 additional sites (Supplementary Fig. S6B and S6C). Interestingly, these UTX binding sites were not enriched for lineage-specific enhancers (Supplementary Fig. S6C). We also confirmed that the MI-503–dependent enrichment of UTX on chromatin was not simply the result of increased *Utx* expression or UTX protein stability (Fig. 2C and D). These data show that disruption of the Menin–MLL1 interaction leads to dynamic recruitment of UTX to promoter regions (Fig. 2B), implying a previously unrecognized functional role for the MLL3/4–UTX complex in promoter regulation in leukemia.

Intriguingly, promoter regions that became uniquely occupied by UTX significantly overlapped with those where Menin was lost, suggesting a dynamic molecular mechanism between these complexes at a subset of gene promoters (Fig. 2E and F; Supplementary Fig. S6D). Correlation analysis also suggested that reduction of Menin binding by MI-503 coincided with increased UTX chromatin occupancy at the same genomic loci (Supplementary Fig. S6E). Comparing UTX chromatin-binding between MLL-AF9 cells and normal hematopoietic stem/progenitor cells revealed that UTX occupies a unique set of binding sites in leukemia cells under basal conditions. On the other hand, MI-503 treatment led to more permissive binding, including to the majority of sites bound in non–*MLL*-r cells, supporting the concept that MLL1–Menin complexes restrict UTX binding in MLL-FP–driven leukemia (Supplementary Fig. S6F). Treatment of mouse fibroblasts (that are not dependent on Menin) with MI-503 did not force UTX mobilization or binding to promoters, indicating that this molecular switch was specific to Menin-dependent cells (Supplementary Fig. S7A–S7E).

The above results indicate that Menin inhibition displaces MLL1–Menin transcriptional regulatory complexes from promoters, enabling UTX to bind and potentially regulate target gene expression (Fig. 2). In agreement, analysis of the chromatin-binding profiles of their cognate H3K4 methyltransferases and their enzymatic histone modifications (Supplementary Fig. S8A and S8B) revealed that Menin–MLL1 inhibition led to a significant decrease in MLL1 chromatin enrichment and a concomitant decrease of its enzymatic product, H3K4me3 (Supplementary Fig. S8C–S8E). In contrast, Menin–MLL1 inhibition led to increased enrichment of the MLL3/4 enzymes at promoter regions co-occupied by UTX and a concomitant increase in H3K4me1 signal at these same loci (Supplementary Fig. S8C, S8F, and S8G). Of note, these loci are distinct from those known to be bound and regulated by the MLL-FPs (ref. 30; Supplementary Fig. S9A–S9E). These data indicate that disruption of the MLL1–Menin interaction induces targeting of the core enzymatic subunits of the

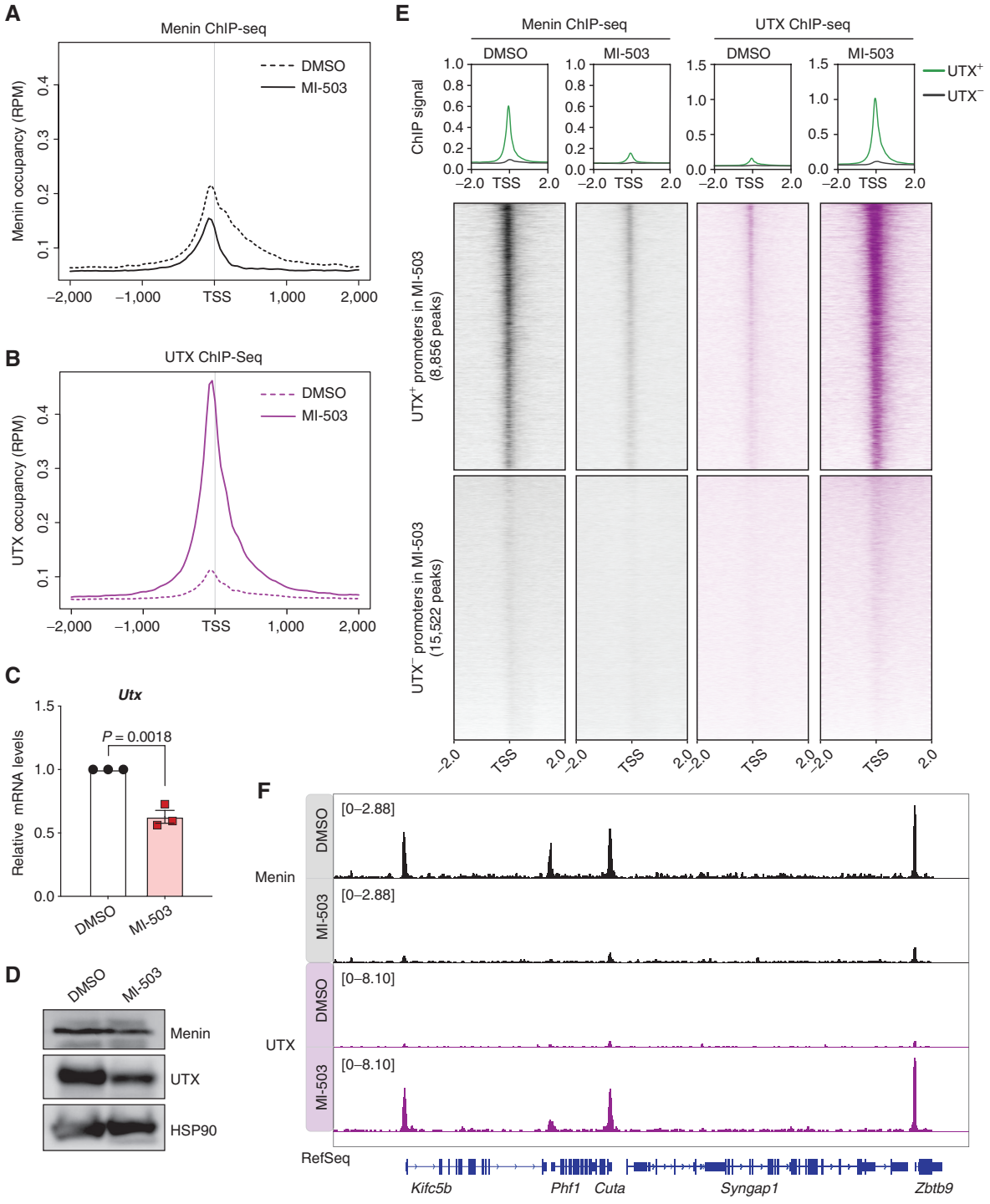

Figure 2. MLL1–Menin complex restricts chromatin occupancy of MLL3/4–UTX at promoters of target genes. **A,** Metagene analysis showing the average chromatin occupancy of Menin at the TSS, and a region 2,000 bp downstream and upstream of the TSS. Signals corresponding to cells treated with a Menin–MLL inhibitor (MI-503, solid) compared with cells treated with vehicle (DMSO, dotted) for 96 hours are shown. RPM, reads per million. **B,** Metagene analysis showing the average chromatin occupancy of UTX at the TSS, and a region 2,000 bp downstream and upstream of the TSS. Signals corresponding to cells treated with a Menin–MLL inhibitor (MI-503, solid) compared with cells treated with vehicle (DMSO, dotted) for 96 hours are shown. **C,** Relative *Utx* mRNA levels determined by qPCR in mouse MLL-AF9 leukemia cells treated with a Menin–MLL inhibitor (MI-503, red) compared with vehicle (DMSO, black) for 96 hours (mean ± SEM, $n = 3$ replicates, P value calculated by Student t test). **D,** Immunoblot analysis of Menin, UTX, and HSP90 proteins (loading control) upon Menin–MLL inhibitor (MI-503) treatment of mouse MLL-AF9 leukemia cells for 96 hours. **E,** Heat maps displaying Menin (black) and UTX (purple) ChIP-seq signals mapping to a 4-kb window around the TSS. Data are shown for DMSO and MI-503–treated cells for 96 hours. Metagene plot shows the average ChIP-seq signal for Menin or UTX at promoters that are UTX$^+$ (green) or UTX$^-$ (black) after MI-503 treatment. **F,** Genome browser representation of ChIP-seq normalized reads for Menin (black) and UTX (purple) in mouse MLL-AF9 leukemia cells treated with either vehicle (DMSO) or a Menin–MLL inhibitor (MI-503) for 96 hours.

MLL3/4–UTX complex to noncanonical sites that are normally bound by the MLL1–Menin complex.

Promoter-associated H3K4me1 has been shown to facilitate transcriptional repression in other cellular settings (54), suggesting that deposition of H3K4me1 at gene promoters could depend on context (55). To determine the functional implications of the Menin–MLL inhibitor–induced colocalization of UTX, MLL3/4, and H3K4me1 at target gene promoters, we leveraged the H3 lysine-4-to-methionine (K4M) "oncohistone" mutant as an orthogonal molecular tool to destabilize and alter the function of the MLL3/4–UTX complex (ref. 56; Supplementary Fig. S10A). Expression of H3.1K4M in MLL-AF9 leukemia cells led to a proliferative advantage only in the context of Menin–MLL inhibition (Supplementary Fig. S10B–S10D), demonstrating that destabilization of the MLL3/4–UTX complex (Supplementary Fig. S10E) can phenocopy the intrinsic resistance of *Utx*-, *Mll3*-, or *Mll4*-deficient cells to Menin–MLL inhibition (Fig. 1E; Supplementary Fig. S3E–S3G). These results further support a model whereby the MLL3/4–UTX complex serves as a context-specific and central modulator of therapy response to Menin–MLL inhibition in leukemia cells.

NF-YA Contributes to Genomic Specificity of the Menin–UTX Molecular Switch on Chromatin

Because Menin lacks a defined DNA binding domain (57), we tested whether a sequence-specific DNA binding factor may regulate the switch between MLL1–Menin and MLL3/4–UTX occupancy at specific promoters. Motif analysis on the genomic regions bound by Menin and UTX in leukemia cells and fibroblasts revealed that NF-Y sequence motifs were the most significantly and selectively enriched in MLL-AF9 leukemia cells (Fig. 3A; Supplementary Fig. S11A and S11B). In agreement, ChIP-seq analysis for NF-YA (the DNA binding and transactivation subunit of the NF-Y complex; ref. 58) showed that it co-occupies sites reciprocally bound by Menin and UTX (Fig. 3B; Supplementary Fig. S11C). Furthermore, Menin–MLL inhibition did not affect NF-YA protein levels, but it decreased NF-YA binding to chromatin (Fig. 3B and C; Supplementary Fig. S11D). To determine how changes in NF-YA genomic binding relate to changes in Menin, UTX, and MLL3/4 chromatin binding in the context of Menin–MLL inhibition, we performed correlation analysis of these ChIP-seq datasets. We found that genomic loci where NF-YA and Menin signals are depleted the most are also regions of high UTX and MLL3/4 enrichment in cells treated with the Menin–MLL inhibitor (Supplementary Fig. S11E). This pattern was evident both genome-wide and more locally at promoters (TSSs). These results support a model whereby Menin and NF-YA colocalize at certain genomic loci that become available for binding by the MLL3/4–UTX complex in the context of Menin–MLL inhibition.

To dissect the relationship between Menin, UTX, and NF-YA, we generated *Nfya*^{KO} MLL-AF9 leukemia cells and treated them with MI-503 (Supplementary Fig. S12A). Disruption of *Nfya* significantly decreased the viability of MI-503–treated leukemia cells at two different time points, suggesting a functional relationship between *Nfya* and *Men1* (Fig. 3D; Supplementary Fig. S12B). Moreover, treatment of *Nfya*^{KO} cells with MI-503 led to a significant increase in UTX occupancy at genomic regions normally bound by Menin and NF-YA at steady state (Fig. 3E; Supplementary Fig. S12C). Collectively, these results implicate NF-Y as one of the sequence-specific transcription factors that marks Menin–UTX target sites and potentially plays a functional role in mediating the Menin–UTX switch at these loci.

Transcriptional Coregulation of Tumor-Suppressive Pathways by a Menin–UTX Molecular Switch

To further probe the molecular phenotypes regulated by this epigenetic switch, we performed transcriptional profiling of MLL-AF9 leukemia cells treated with MI-503 and identified pathways that are reciprocally regulated by Menin and UTX. Although the activity of the MLL1–Menin complex is associated with actively transcribed developmental genes (2, 13), MI-503 treatment resulted in both up- and downregulation of gene expression, with the majority of significantly upregulated genes reciprocally bound by Menin and UTX (Fig. 4A and B).

To gain further insights into the mechanism, we performed ChIP-seq against acetylated H3K27 and H4K16 (H3K27ac and H4K16ac; histone modifications associated with gene activation; ref. 59) and found that the levels of these modifications increased at sites where the MLL3/4–UTX complex is enriched upon Menin–MLL inhibition (Supplementary Fig. S13A and S13B). These loci also showed increased binding of MOF, a histone H4K16 acetyltransferase (Supplementary Fig. S13C; refs. 60–62). Thus, Menin–MLL inhibition produces dynamic changes in gene expression due to loss of MLL1–Menin-dependent repressive activity and a concomitant increase in histone modifications associated with gene activation (including H4K16ac and H3K27ac; refs. 63, 64).

To determine if UTX was necessary for gene activation, we generated *Utx*^{KO} MLL-AF9 leukemia cells, treated these with MI-503, and profiled them by RNA sequencing (RNA-seq; Supplementary Fig. S14A and S14B). We found that genes bound by Menin and UTX that are induced by MI-503 failed to get activated in *Utx*^{KO} cells, suggesting UTX function is necessary for their transcriptional activation upon Menin displacement from chromatin (we refer to these genes as "Menin–UTX targets"; Fig. 4C; Supplementary Table S4). Consistent with the idea that this mechanism is independent of the MLL-FP, we found that MI-503-treated *Utx*^{KO} cells still exhibited downregulation of canonical MLL–AF9 targets and induction of myeloid differentiation programs (Supplementary Fig. S15A–S15C), as has been observed in *Utx*^{WT} cells (22, 25, 27). Moreover, these cells were able to proliferate without reexpression of *Meis1* and *Hoxa9*—two critical Menin–MLL-FP targets (Fig. 1E; Supplementary Figs. S5G and S15D; refs. 25, 27, 51, 52). These data suggest a new paradigm whereby the effects of Menin–MLL inhibition on MLL-FP target genes are independent of its effects on Menin–UTX transcriptional targets, and that concomitant induction of tumor-suppressive gene expression programs and repression of canonical MLL-FP targets are required for the antileukemic activity of Menin–MLL1 inhibitors.

To gain insight into cellular and molecular pathways regulated by the Menin–UTX switch, we performed gene ontology analysis (65, 66) of Menin–UTX targets and found

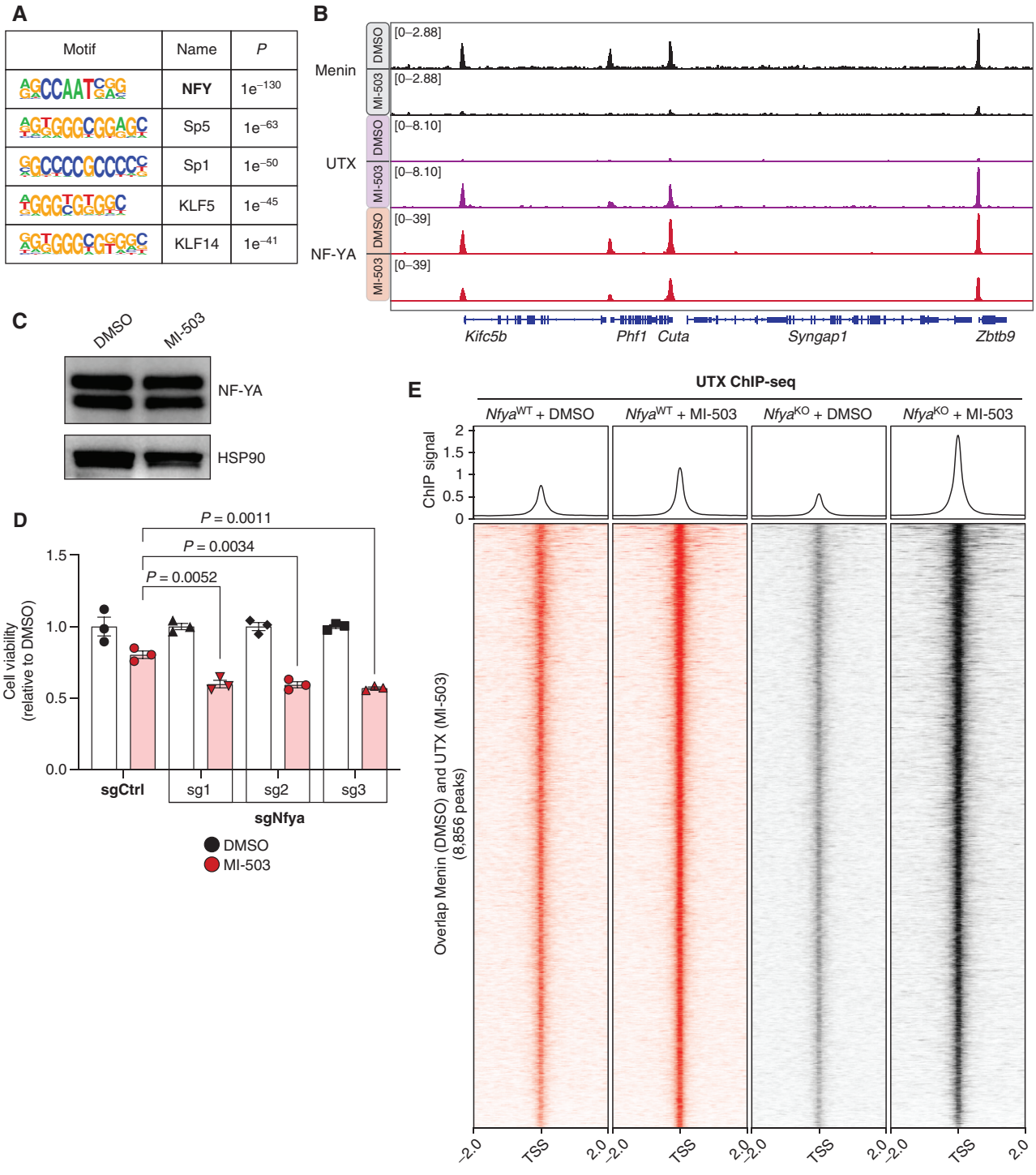

Figure 3. NF-YA contributes to genomic specificity of the Menin–UTX molecular switch on chromatin. **A,** HOMER *de novo* motif analysis of overlapping ChIP-seq peaks between Menin (in DMSO) and UTX (in MI-503) in mouse MLL-AF9 leukemia cells. **B,** Genome browser representation of ChIP-seq normalized reads [average reads per kilobase per million mapped reads (RPKM)] for representative loci bound by Menin (black), UTX (purple), and NF-YA (red) in cells treated with vehicle (DMSO) or a Menin–MLL inhibitor (MI-503) for 96 hours. **C,** Immunoblot analysis of NF-YA and HSP90 proteins (loading control) upon Menin–MLL inhibitor (MI-503) treatment of mouse MLL-AF9 leukemia cells for 96 hours. **D,** Viability assay from cells treated with vehicle (DMSO, black) or a Menin–MLL inhibitor (MI-503, red) for 96 hours (mean ± SEM, $n = 3$ infection replicates, *P* values calculated by Student *t* test). sgCtrl, control sgRNA targeting a nongenic region on chromosome 8. **E,** Heat maps displaying UTX ChIP-seq signal mapping to a 4-kb window around the TSS in *Nfya*^{WT} (red) or *Nfya*^{KO} (black) mouse MLL-AF9 leukemia cells treated with vehicle (DMSO) or a Menin–MLL inhibitor (MI-503) for 96 hours. Metaplot represents the average UTX ChIP-seq signal at promoters.

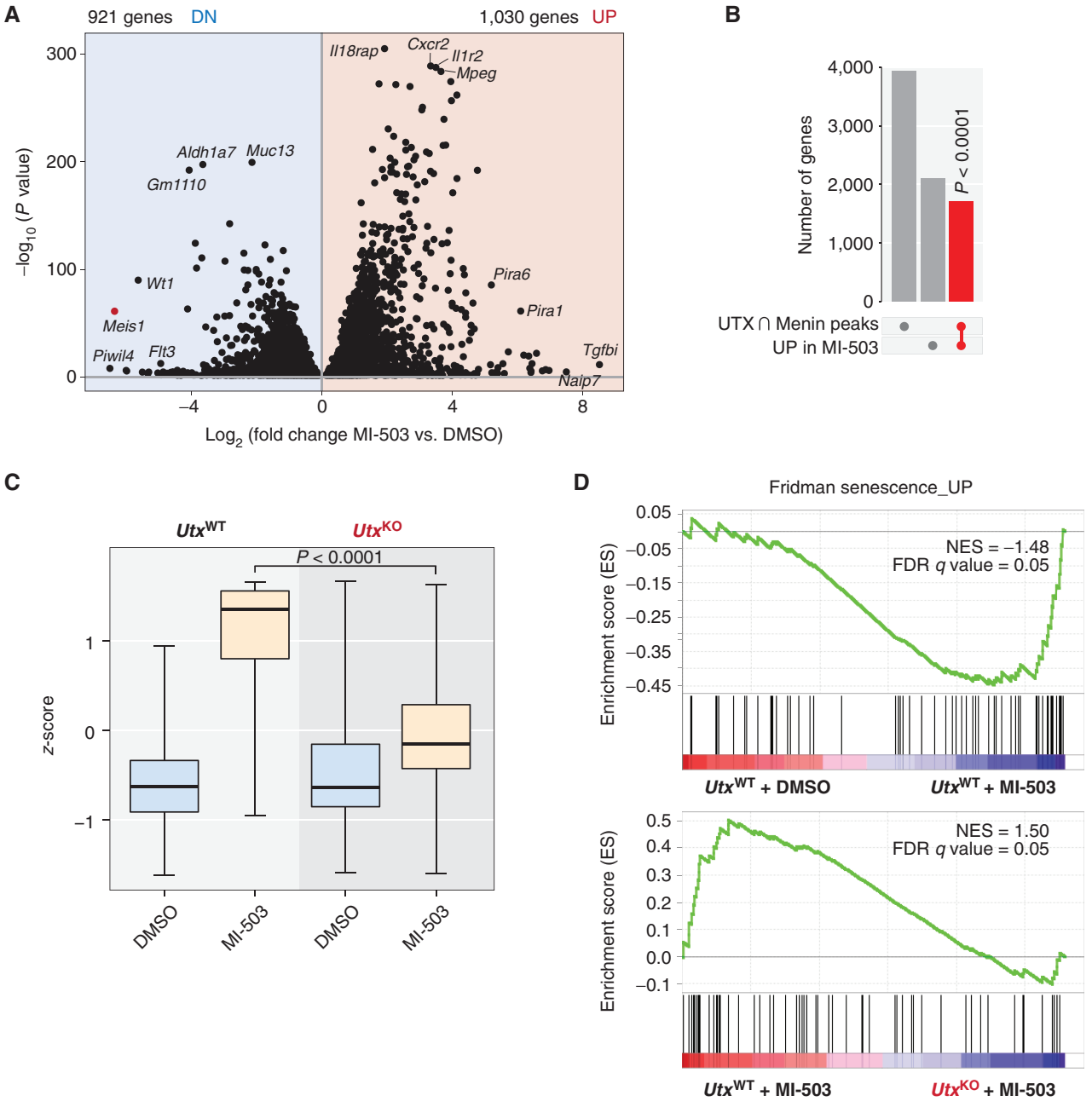

Figure 4. Transcriptional coregulation of tumor-suppressive pathways by the Menin–UTX switch. **A,** Volcano plot of differentially expressed genes in mouse MLL-AF9 leukemia cells treated with a Menin–MLL inhibitor (MI-503) or vehicle (DMSO) for 96 hours. Significantly ($P < 0.05$) downregulated (DN) genes are shown on the left ($n = 921$ genes). Significantly ($P < 0.05$) upregulated (UP) genes are shown on the right ($n = 1{,}030$). **B,** Upset plot showing significant overlap (red) between genes that undergo replacement of Menin by UTX at their promoters and MI-503–induced genes. *P* value for overlap is shown. **C,** Box plot showing expression levels of genes that are induced by Menin–MLL inhibitor (MI-503) treatment and are bound by UTX at their promoters in this condition and by Menin at steady state. Expression levels are shown for Utx^{WT} and Utx^{KO} leukemia cells. The midline in box plots represents median. *P* value for MI-503 comparison is shown. **D,** GSEA showing that a Menin–UTX targets induced by a Menin–MLL inhibitor (MI-503) are significantly enriched for genes regulating cellular senescence. FDR, false discovery rate; NES, normalized enrichment score. (*continued on following page*)

significant evidence for their association with transcriptional programs related to proliferation, differentiation, and survival (Supplementary Fig. S16A; Supplementary Table S4). To further evaluate the relevance of these gene ontology terms, we performed gene set enrichment analysis (GSEA; ref. 67) on transcriptional data from MI-503-treated Utx^{WT} and Utx^{KO} cells and observed a significant correlation between the presence of UTX and the expression of senescence-associated genes following treatment (Fig. 4D; Supplementary Fig. S16B–S16G; Supplementary Table S4; ref. 68). This correlation was also observed when we analyzed a curated list of genes involved in cell-cycle arrest and therapy-induced senescence (Fig. 4E;

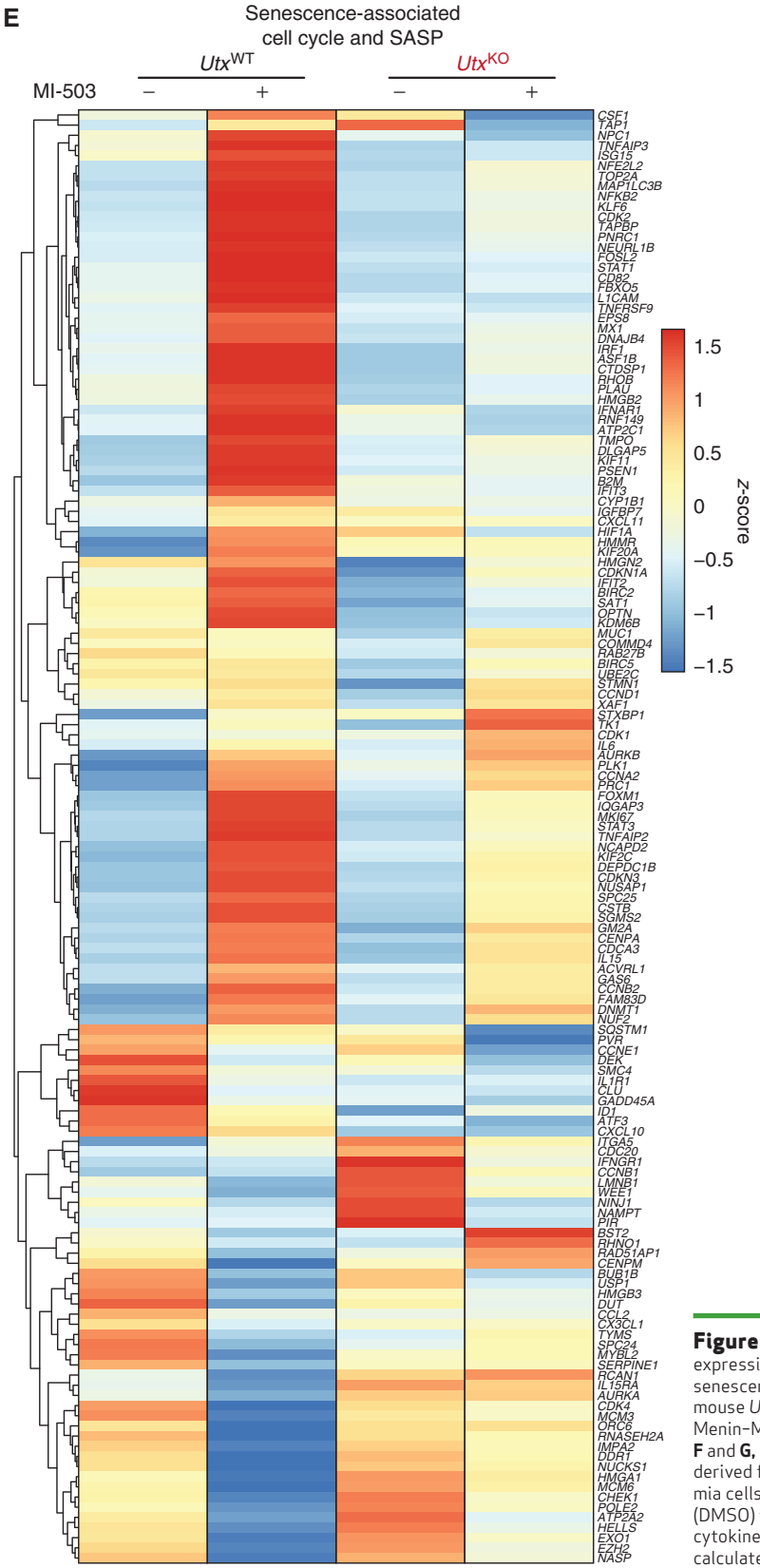

Figure 4. ***(Continued)*** **E,** Heat map showing relative gene expression levels of senescence-associated cell-cycle and senescence-associated secretory phenotype (SASP) genes in mouse *Utx*^{WT} and *Utx*^{KO} MLL-AF9 leukemia cells treated with a Menin–MLL inhibitor (MI-503) or vehicle (DMSO) for 96 hours. **F** and **G,** Secreted levels of IL6 and IFNβ-1 in conditioned media derived from mouse *Utx*^{WT} (black) and *Utx*^{KO} (red) MLL-AF9 leukemia cells treated with a Menin–MLL inhibitor (MI-503) or vehicle (DMSO) for 4 or 6 days. Data are quantified as pg/mL of secreted cytokine per million cells (mean ± SEM, $n = 3$ replicates, P values calculated by Student t test).

ref. 69). These transcriptional changes are consistent with the fact that Menin–MLL inhibition induces a combination of cell-cycle arrest, apoptosis, and differentiation (Supplementary Fig. S1E–S1G; ref. 22), as well as our observation that the senescence-associated H4K16ac modification increases with MI-503 treatment (Supplementary Fig. S13B and S13C; ref. 70). To gain additional insights into senescence-associated gene activation mechanisms, we performed ChIP-seq for RNA polymerase II and observed increased occupancy at the promoters of senescence-associated genes that are upregulated by MI-503 treatment (Supplementary Fig. S16H). Thus, the interplay between Menin and UTX in the context of Menin–MLL inhibition regulates the expression of genes involved in cell-cycle arrest and senescence.

The cellular senescence program is highly complex and characterized in part by induction of permanent cell-cycle arrest and a senescence-associated secretory phenotype (SASP; ref. 71). To determine if Menin–MLL inhibition induces SASP, we measured cytokine and chemokine levels in conditioned media from MLL-AF9 leukemia cells treated with MI-503. Secretion of prototypical SASP cytokines such as IL6, IFNβ-1, IL3, and IL15 was induced upon Menin–MLL inhibition in a *Utx*-dependent manner, supporting a direct role for the Menin–UTX switch in regulating cellular senescence (Fig. 4F and G; Supplementary Fig. S17A–S17C). Thus, Menin–MLL inhibition engages a tumor-suppressive network that includes therapy-induced cellular senescence and is regulated by the MLL3/4–UTX complex.

The Enzymatic Domain of UTX Is Dispensable for Tumor-Suppressive Functions in Response to Menin–MLL Inhibition

The UTX protein contains several functional domains, including a JmjC histone demethylase domain that catalyzes the removal of the H3K27me3 modification (72–75). To determine the regions of UTX that are necessary for treatment-associated UTX-dependent phenotypes, we performed structure–function–rescue experiments in Utx^{KO}-null leukemia cells using lentiviral constructs encoding dual N-terminal HA- and C-terminal FLAG-tagged truncations of UTX (Fig. 5A; Supplementary Fig. S18A–S18C). Full-length UTX or a UTX truncation harboring the first 500 amino acids ($UTX^{1–500}$) and lacking the JmjC demethylase domain (72–75) was sufficient to resensitize cells to MI-503 treatment whereas truncations proximal to the C-terminus were unable to do so (Fig. 5B). Consistent with these cellular phenotypes, full-length UTX and $UTX^{1–500}$ were sufficient to rescue UTX-dependent transcriptional phenotypes associated with Menin–MLL inhibition (Fig. 5C), including induction of Menin–UTX target genes (Fig. 5D; Supplementary Fig. S19). These results demonstrate that an N-terminal truncation of UTX, lacking the JmjC demethylase domain and a recently reported intrinsically disordered region (76), is both necessary and sufficient to drive treatment-associated tumor-suppressive responses.

To further confirm that UTX uses noncatalytic mechanisms to regulate gene expression in the context of Menin–MLL inhibition, we performed ChIP-seq for H3K27me3, a modification catalyzed by PRC2 (77) and removed by UTX (72–75). We found that the genomic redistribution of UTX induced upon treatment with MI-503 (Fig. 2B and E) did not affect global levels or distribution of H3K27me3 (Supplementary Fig. S20A and S20B), suggesting that this histone modification might not play a critical role in these phenotypes. To functionally test this possibility, we generated isogenic $Ezh2^{KO}$;Utx^{WT} and $Ezh2^{KO}$;Utx^{KO} MLL-AF9 leukemia cells and confirmed the absence of H3K27me3 by immunoblotting (Supplementary Fig. S20C). Consistent with our model, $Ezh2^{KO}$;Utx^{WT} leukemia cells remained exquisitely sensitive to MI-503, whereas $Ezh2^{KO}$;Utx^{KO} cells were resistant to Menin–MLL inhibition (Supplementary Fig. S20D). These results demonstrate that the catalytic domain of UTX is dispensable for UTX-dependent phenotypes and therapeutic responses to Menin–MLL inhibitors.

Combinatorial Targeting of Menin and CDK4/6 Overcomes Resistance Associated with MLL3/4–UTX Dysfunction

Senescence can be regulated at both transcriptional and posttranscriptional levels, and chromatin regulation has been functionally implicated in modulating these programs (70, 78, 79). We examined whether the Menin–UTX molecular switch directly regulates the expression of cell-cycle arrest and senescence–associated genes by direct binding to their promoters (80, 81). Consistent with this model, we found that Menin is bound to the promoters of the cyclin-dependent kinase (CDK) inhibitors *Cdkn2c/Ink4c* and *Cdkn2d/Ink4d* at basal conditions (82), and that enrichment is decreased upon Menin–MLL inhibition, coinciding with their increased expression (Fig. 6A; Supplementary Fig. S21A–S21C). Conversely, we found that UTX binds to these promoters only in the context of Menin–MLL inhibition, leading to UTX-dependent upregulation of both CDK inhibitors (Fig. 6A and B). Thus, the Menin–UTX molecular switch regulates the expression of these CDK inhibitors by direct chromatin regulation.

Because the proteins encoded by these two genes are natural inhibitors of the CDK4 and CDK6 kinases (82), we tested whether pharmacologic inhibition of CDK4/6 could bypass the intrinsic resistance of Utx^{KO} cells to MI-503 while retaining the therapeutic effects of Menin–MLL inhibition on MLL-FP targets (Fig. 6C). Treatment of MLL-AF9 leukemia cells with MI-503 and the FDA-approved CDK4/6 inhibitor palbociclib (83) showed that Utx^{KO} cells were more resistant to either MI-503 or palbociclib alone relative to Utx^{WT} cells, likely due to higher basal levels of *Cdk6* transcripts (Fig. 6D; Supplementary Fig. S21D; refs. 80, 84). However, combined inhibition of Menin–MLL and CDK4/6 resulted in a synergistic effect (CD = 0.4; ref. 85) on inhibiting cell proliferation to levels similar to those achieved by MI-503 treatment of Utx^{WT} cells (Fig. 5D). These results demonstrate that targeting pathways regulated by Menin and UTX can produce combinatorial therapeutic effects and suggest that the antileukemic effects of MI-503 (22) are primarily through reactivation of tumor suppressor pathways and not solely through dampening transcription of MLL-FP targets like *Meis1* (refs. 22, 25, 27, 51; Supplementary Fig. S5G and S15D). Thus, the combination of palbociclib with Menin–MLL inhibitors may represent a novel and more effective therapeutic strategy for Menin-dependent cancers (23, 24, 26, 86).

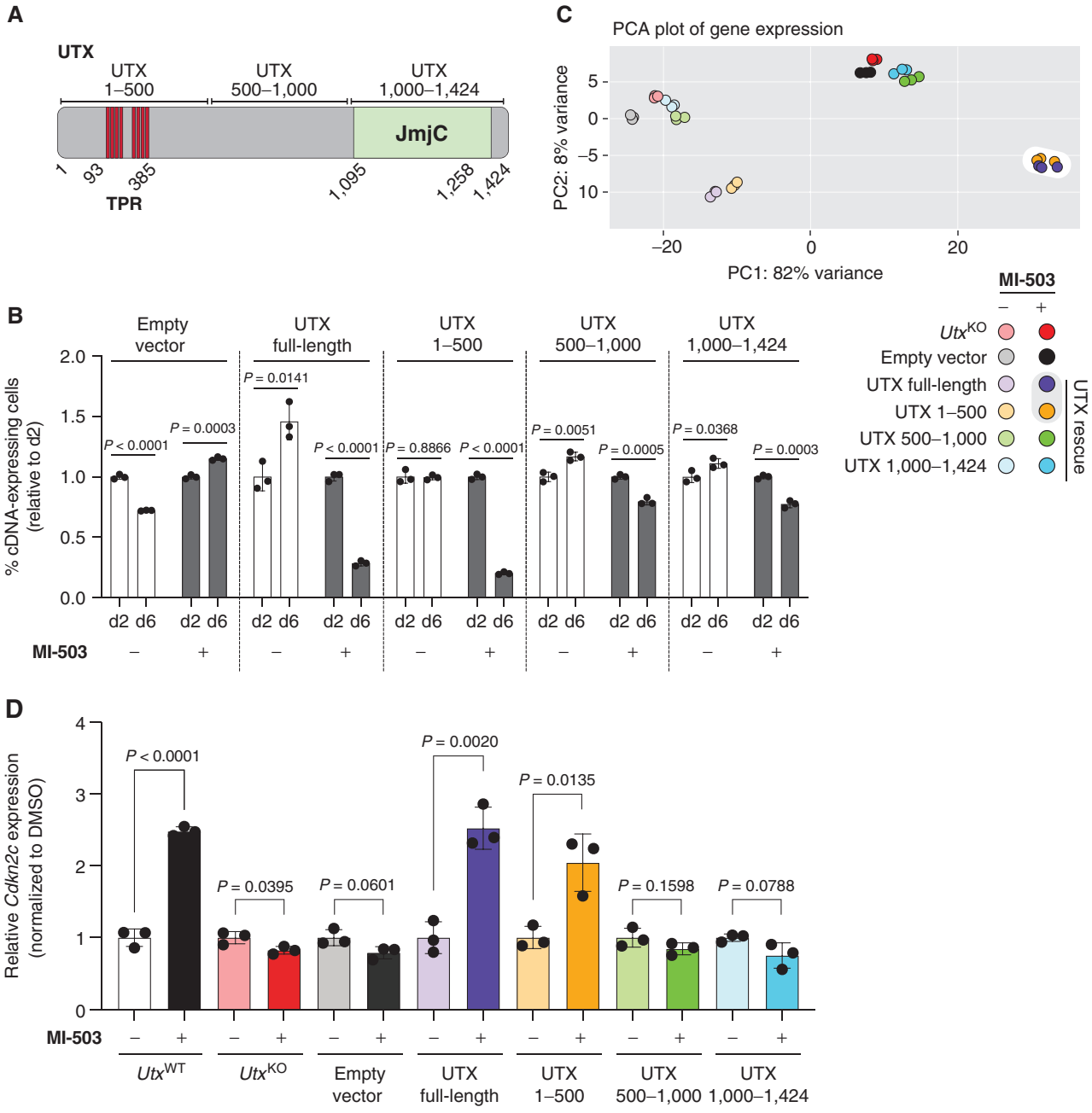

Figure 5. Enzymatic domain of UTX is dispensable for its tumor-suppressive functions in response to Menin–MLL inhibition. **A,** Schematic of UTX protein. Highlighted are the 8 tetratricopeptide repeats (TPR; 93–385 aa) and the histone demethylase (JmjC) domain (1,095–1,258aa). Three ~500 amino-acid-long truncations are also represented. **B,** Growth competition assay in mouse *Utx*^{KO} MLL-AF9 leukemia cells expressing different RFP-tagged *Utx* cDNAs and treated with Menin–MLL inhibitor (MI-503) for 2 or 6 days. The graph shows the relative growth of leukemia cells infected with RFP-tagged *Utx* cDNAs measured by flow cytometry (mean ± SEM, $n = 3$ infection replicates, *P* values calculated by Student *t* test). **C,** Principal component analysis (PCA) of gene expression data from *Utx*^{KO} MLL-AF9 leukemia cells expressing different RFP-tagged *Utx* cDNAs and treated with vehicle (DMSO) or Menin–MLL inhibitor (MI-503) for 96 hours. **D,** *Cdkn2c* expression (mean normalized read counts) from different *Utx* truncations in mouse MLL-AF9 leukemia cells treated with vehicle (DMSO) or a Menin–MLL inhibitor (MI-503) for 96 hours (mean ± SEM, $n = 3$ replicates, *P* values calculated by Student *t* test).

In Vivo Response to Menin–MLL Inhibitors Is Accompanied by Induction of MLL3/4–UTX-Dependent Tumor-Suppressive Programs

Small-molecule inhibitors of the Menin–MLL interaction have shown significant promise in preclinical models of acute lymphoid and myeloid leukemias (25, 87) and are currently in phase II clinical trials for treatment of patients with acute leukemia [SNDX-5613 (NCT04067336), KO-539 (NCT04065399), and JNJ-75276617 (NCT04811560)]. Notably, SNDX-5613 was recently granted fast-track designation by the FDA for the treatment of relapsed/refractory acute leukemias. To examine whether the Menin–UTX molecular

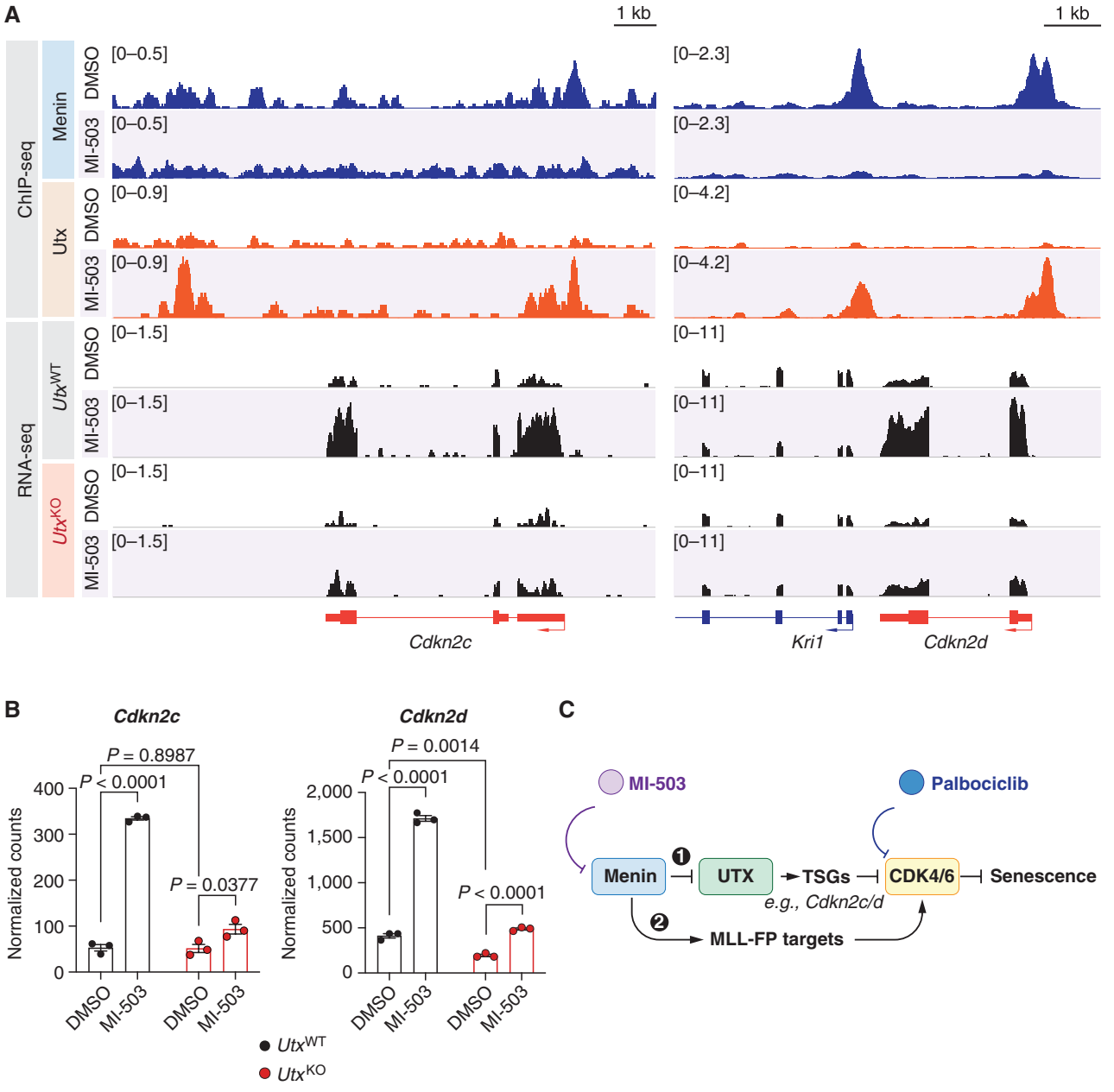

Figure 6. Combinatorial targeting of Menin and CDK4/6 overcomes resistance associated with MLL3/4 dysfunction. **A,** Genome browser representation of ChIP-seq (top) and RNA-seq (bottom) normalized reads [average reads per kilobase per million mapped reads (RPKM)] for *Cdkn2c* and *Cdkn2d* loci from mouse *Utx*^{WT} or *Utx*^{KO} MLL-AF9 leukemia cells treated with vehicle (DMSO) or a Menin–MLL inhibitor (MI-503) for 96 hours. **B,** *Cdkn2c* and *Cdkn2d* expression (mean normalized read counts) from mouse *Utx*^{WT} (black) and *Utx*^{KO} (red) MLL-AF9 leukemia cells treated with vehicle (DMSO) or a Menin–MLL inhibitor (MI-503) for 96 hours (mean ± SEM, $n = 3$ replicates, *P* values calculated by Student *t* test). **C,** Proposed model and rationale for combination therapies based on Menin–MLL and CDK4/6 inhibitors. Our data support a model whereby (1) Menin restricts UTX-mediated transcriptional activation of tumor suppressor genes (TSG), including *Cdkn2c* and *Cdkn2d*, which are natural inhibitors of the CDK4 and CDK6 kinases, which in turn inhibit cell-cycle arrest and senescence. Our model predicts that CDK4/6 inhibition using palbociclib should boost the anticancer activity of Menin–MLL inhibitors, which we show induces an MLL3/4–UTX tumor-suppressive axis, by more potently inhibiting these downstream kinases. On the other hand, Menin is known to be required for the activation of MLL-FP targets like *Meis1* and *Cdk6* itself to sustain leukemia (2). Our model predicts that combination therapies based on Menin–MLL and CDK4/6 inhibitors should act synergistically to suppress leukemia proliferation by potently engaging two parallel pathways that converge on regulation of cell-cycle progression. (*continued on following page*)

switch described above is operative in patients with leukemia treated with Menin–MLL inhibitors, we performed longitudinal RNA-seq analysis of primary AML cells derived from two patients with *NPM1c*-mutated (patient 1) and *MLL*-r (patient 2) leukemia treated with SNDX-5613 (AUGMENT-101 clinical trial; NCT04065399; Fig. 7A; Supplementary Fig. S22A). Consistent with our hypothesis, SNDX-5613 led to concomitant suppression of canonical MLL-FP target genes

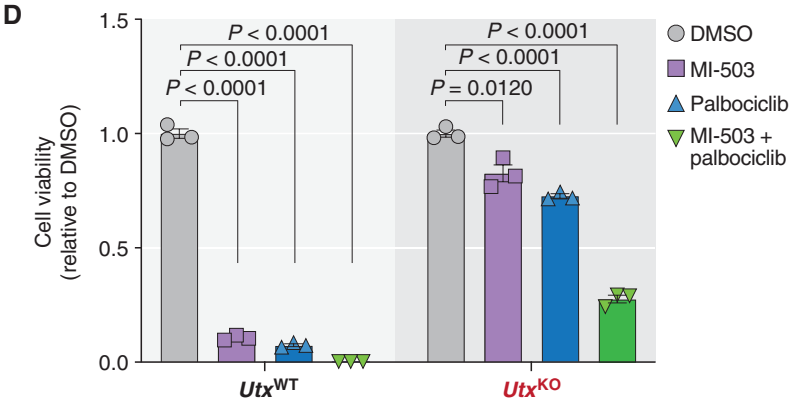

Figure 6. ***(Continued)*** **D,** Relative viability of Utx^{WT} and Utx^{KO} MLL-AF9 leukemia cells treated with either vehicle (DMSO), a Menin–MLL inhibitor (MI-503), a CDK4/6 inhibitor (palbociclib), or a combination of both inhibitors for 6 days (mean ± SEM, $n = 3$ replicates, P values calculated by Student t test).

(e.g., *MEIS1*) and induction of Menin–UTX targets including CDK inhibitors (e.g., *CDKN2C*; Fig. 7B–E; Supplementary Fig. S22B and S22C).

As an orthogonal approach, we analyzed the *in vivo* response and resistance of *MLL*-r acute leukemia patient-derived xenografts (PDX) to VTP-50469 (a close analogue of SNDX-5613; Fig. 7F; Supplementary Fig. S23A and S23B; ref. 25). Consistent with our model, mice transplanted with an *MLL3* wild-type PDX showed a potent therapeutic response to VTP-50469 and transcriptional induction of Menin–UTX targets (Fig. 7G and H; Supplementary Fig. S24A). Conversely, an *MLL3*-mutant PDX exhibited primary resistance to VTP-50469 and failed to induce this gene expression program (Fig. 7I and J; Supplementary Fig. S24A), linking the induction of Menin–UTX targets to preclinical drug response. Thus, gene expression programs regulated by MLL1–Menin and MLL3/4–UTX complexes are operative in patients with AML and PDX models treated with orally bioavailable Menin–MLL inhibitors that are currently under clinical investigation.

To test whether CDK4/6 inhibition can overcome the blunted induction of endogenous CDK inhibitors in the context of Menin inhibitor resistance, we treated mice harboring the *MLL3*-mutant AML PDX with VTP-50469 and palbociclib (Fig. 7K). Although single treatment with Menin or CDK4/6 inhibitors led to a minor decrease in leukemia burden in the bone marrow of recipient mice after 10 days of treatment, combination treatment with VTP-50469 and palbociclib induced significant leukemia regression (Fig. 7K and L). Moreover, RNA-seq from human leukemia cells isolated from these animals showed induction of cell-cycle arrest and senescence–associated gene expression signatures in mice treated with both VTP-50469 and palbociclib (Fig. 7M; Supplementary Fig. S24B and S24C). Altogether, these data provide preclinical evidence for the feasibility and efficacy of combined Menin and CDK4/6 inhibition to overcome the blunted induction of senescence-associated programs in patient-derived leukemias resistant to Menin inhibitor monotherapy.

DISCUSSION

The chromatin adapter protein Menin exhibits context-specific functions in different tissues, acting as a tumor suppressor gene in neuroendocrine (14, 15), lung (17, 88), skin (16), and CNS (18) malignancies and as an oncogenic cofactor in hepatocellular (19) and hematologic cancers (4, 20). Menin can interact with similar cofactors in disparate settings, and the biological and molecular basis for these ostensibly paradoxical findings has remained unclear. For example, Menin functionally cooperates with MLL proteins to activate transcription of the *Cdkn1b/p27*^{Kip1} and *Cdkn2d/Ink4d* CDK inhibitors as a tumor-suppressive mechanism in neuroendocrine tumors and lung cancer (3, 17, 89, 90), yet the same protein–protein interaction is critical for leukemia maintenance (4, 10).

Our study sheds light on these paradoxical observations by revealing a functional interaction between the mammalian histone methyltransferase complexes MLL1–Menin and MLL3/4–UTX and, in doing so, challenging the paradigms that (i) these complexes are canonically restricted to certain genomic compartments (some exceptions have been identified; refs. 91–93), and (ii) activation of gene promoters is strictly associated with H3K4me3 deposition, whereas H3K4me1 enrichment at promoters is believed to be associated with repression (Supplementary Fig. S25; refs. 54, 94). In leukemia cells harboring MLL fusions, Menin–MLL1 represses the expression of a tumor-suppressive network that involves *Cdkn2c/Ink4c* and *Cdkn2d/Ink4d* by binding to gene promoters and depositing H3K4me3. Disruption of Menin–MLL1 complexes using genetic or pharmacologic approaches triggers a molecular switch that leads to *de novo* recruitment of the MLL3/4–UTX complex to promoters of tumor-suppressive genes that were previously bound by Menin–MLL. This switch also leads to a UTX-dependent increase in activation-associated histone modifications and gene expression (70, 78). Importantly, these phenotypes are independent of UTX catalytic activity, as the first 500 amino acids of UTX, which lack the histone demethylase domain, are sufficient to rescue UTX deficiency. This finding is particularly interesting given a recent study suggesting that UTX requires a much bigger protein fragment to drive tumor-suppressive activity and transcriptional regulation via phase separation mechanisms (76). Instead, our study demonstrates that UTX does not require a core intrinsically disordered region to drive tumor-suppressive responses in the context of Menin–MLL inhibition. Thus, UTX uses noncatalytic mechanisms to regulate gene expression programs that affect response to epigenetic therapies.

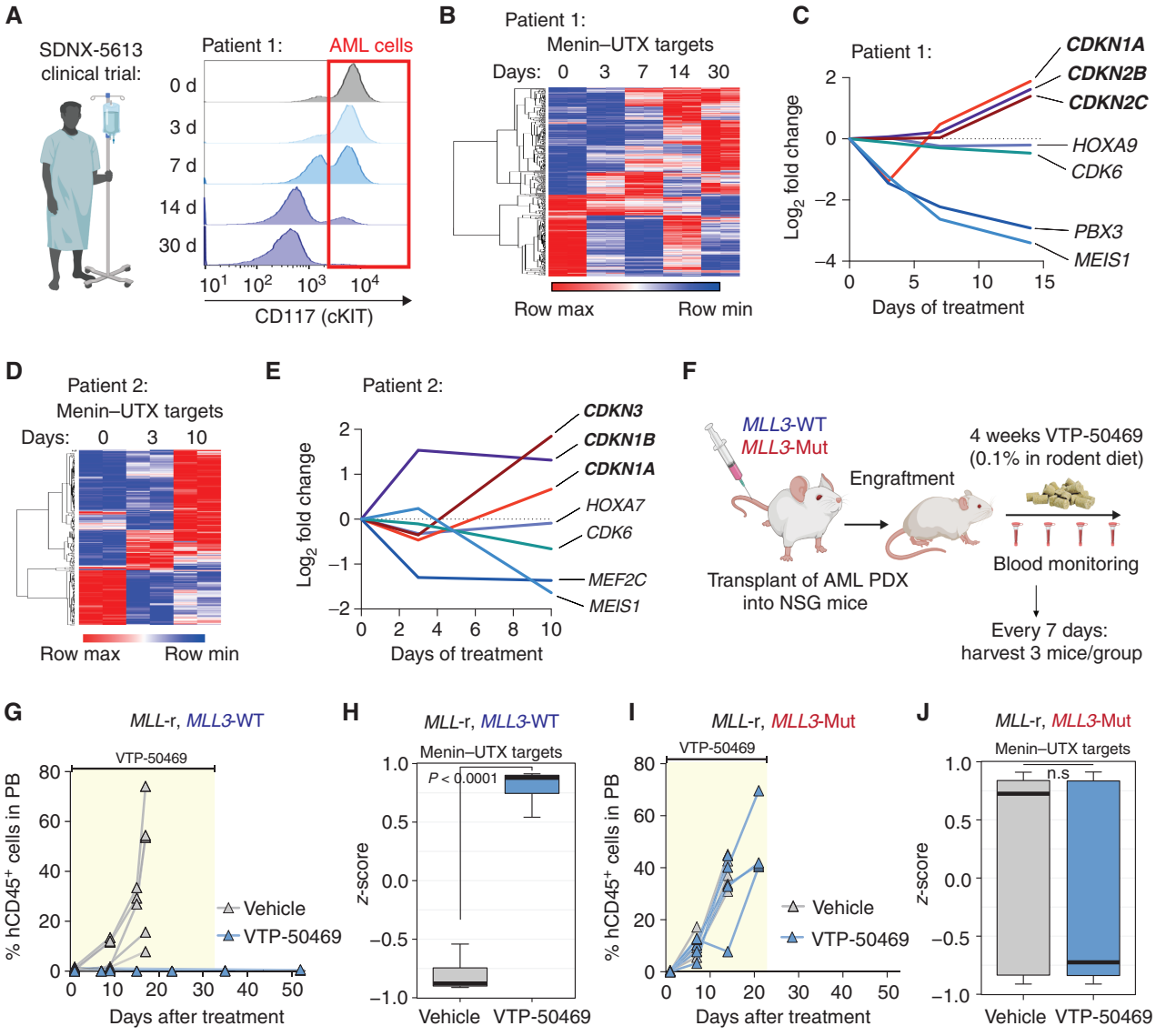

Figure 7. *In vivo* response to Menin–MLL inhibition is accompanied by induction of MLL3/4–UTX-dependent tumor-suppressive programs. **A,** Longitudinal flow cytometry analysis showing the fraction of CD45^{lo}, cKIT^{+} leukemia cells in the peripheral blood of an *NPM1c*-mutant patient (patient 1) during cycle 1 of Menin–MLL inhibitor (SDNX-5613) treatment as part of the AUGMENT-101 clinical trial (NCT04065399). **B,** Temporal gene expression changes for Menin–UTX targets in FACS-sorted leukemia blast cells isolated from patient 1 as part of the AUGMENT-101 clinical trial (NCT04065399). Heat map shows all Menin–UTX targets that are differentially expressed at day 14 versus day 0 of treatment cycle 1. **C,** Temporal expression levels of genes involved in cell-cycle arrest and senescence (*CDKN1A*, *CDKN2B*, and *CDKN2C*) and Menin–UTX targets (*HOXA9*, *CDK6*, *PBX3*, and *MEIS1*) in leukemia blast cells isolated from patient 1 treated with SDNX-5613. **D,** Temporal gene expression changes for Menin–UTX targets in FACS-sorted leukemia blast cells isolated from patient 2 treated with SDNX-5613 as part of the AUGMENT-101 clinical trial (NCT04065399). Heat map shows all Menin–UTX targets that are differentially expressed at day 10 versus day 0 of treatment cycle 1. **E,** Temporal expression levels of genes involved in cell-cycle arrest and senescence (*CDKN1A*, *CDKN1B*, and *CDKN3*) and MLL-FP targets (*HOXA7*, *CDK6*, *MEF2C*, and *MEIS1*) in leukemia blast cells isolated from patient 2 treated with SDNX-5613. **F,** Schematic of *in vivo* treatment experiments using genetically defined AML PDXs. NSG mice were transplanted with either *MLL3* wild-type (*MLL3*-WT) or *MLL3*-mutant (*MLL3*-Mut) AML PDXs and, upon disease engraftment, were randomized into Menin–MLL inhibitor (VTP-50469) or normal chow for a duration of 4 weeks. Disease progression was monitored weekly by bleeding, and AML cells were sorted 7 days after initiation of treatment using magnetic mouse cell depletion from the bone marrow of animals to perform RNA-seq. **G,** Disease progression as measured by the percentage of human CD45^{+} cells in the peripheral blood (PB) of mice harboring *MLL3*-WT leukemia treated with vehicle (gray) or a Menin–MLL inhibitor (VTP-50469, blue). **H,** Box plot denoting gene expression changes of Menin–UTX targets in AML cells isolated from mice harboring *MLL3*-WT leukemia treated with vehicle (gray) or a Menin–MLL inhibitor (VTP-50469, blue). **I,** Disease progression as measured by the percentage of human CD45^{+} cells in the peripheral blood of mice harboring *MLL3*-mutant leukemia treated with vehicle (gray) or a Menin–MLL inhibitor (VTP-50469, blue). **J,** Box plot denoting gene expression changes of Menin–UTX targets in AML cells isolated from mice harboring *MLL3*-mutant leukemia treated with vehicle (gray) or a Menin–MLL inhibitor (VTP-50469, blue). (*continued on following page*)

Our findings have important translational implications, as they shed light on a novel noncanonical gene expression program regulated by Menin. We demonstrate that the Menin–MLL1 complex maintains repression of a set of target genes under steady-state conditions, which only becomes activated upon Menin inhibitor–mediated displacement of

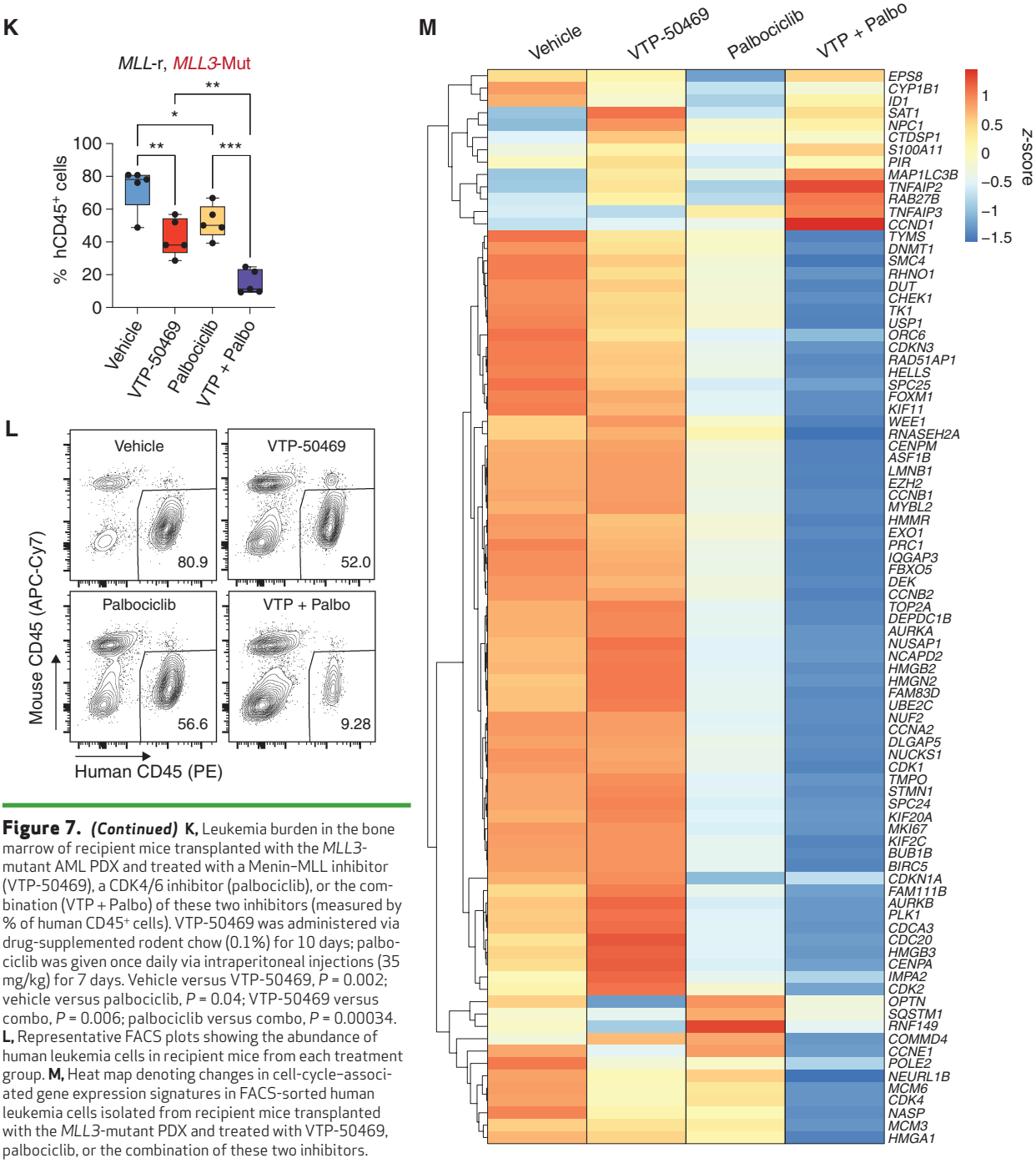

Figure 7. ***(Continued)*** **K,** Leukemia burden in the bone marrow of recipient mice transplanted with the *MLL3*-mutant AML PDX and treated with a Menin–MLL inhibitor (VTP-50469), a CDK4/6 inhibitor (palbociclib), or the combination (VTP + Palbo) of these two inhibitors (measured by % of human CD45$^+$ cells). VTP-50469 was administered via drug-supplemented rodent chow (0.1%) for 10 days; palbociclib was given once daily via intraperitoneal injections (35 mg/kg) for 7 days. Vehicle versus VTP-50469, $P = 0.002$; vehicle versus palbociclib, $P = 0.04$; VTP-50469 versus combo, $P = 0.006$; palbociclib versus combo, $P = 0.00034$. **L,** Representative FACS plots showing the abundance of human leukemia cells in recipient mice from each treatment group. **M,** Heat map denoting changes in cell-cycle–associated gene expression signatures in FACS-sorted human leukemia cells isolated from recipient mice transplanted with the *MLL3*-mutant PDX and treated with VTP-50469, palbociclib, or the combination of these two inhibitors.

MLL1–Menin and recruitment of MLL3/4–UTX. The set of Menin–UTX target genes that we defined here is enriched for genes that are associated with cell-cycle arrest and senescence, and we have shown that their activation is critical for the response to Menin–MLL inhibitors *in vitro* and *in vivo*. Importantly, activation of this Menin–UTX program is observed in human AML subjects in the context of the ongoing AUGMENT-101 phase I clinical trial (NCT04065399), providing the first clinical evidence that both canonical and noncanonical Menin–MLL programs are operative in patients under Menin inhibitor treatment.

The current focus in the field of translational and clinical hematologists focusing on Menin inhibitors as a novel therapeutic agent in *MLL*-r and *NPM1c*-mutant leukemia lies almost exclusively on the direct regulation of canonical MLL-FP targets. Nevertheless, we demonstrate that concurrent repression of canonical MLL-FP targets and activation of the noncanonical Menin–UTX program is required for effective treatment, and that functional inactivation of *UTX*, *MLL3*, or *MLL4* impairs therapeutic responses (Supplementary Fig. S25). We also show that dual targeting of this molecular axis using Menin–MLL and CDK4/6 inhibitors bypasses the requirement

for Menin inhibitor–induced UTX recruitment and has a strong combinatorial effect on leukemia cell proliferation *in vitro* and in a previously nonresponsive leukemia PDX model.

The findings presented here provide a rationale for future biomarker studies investigating whether the induction of Menin–UTX target genes may serve as an early indicator to evaluate if leukemia cells respond robustly to Menin inhibitor treatment. The distinct role of different types of somatic mutations in *MLL3*, *MLL4*, or *UTX*, which are prevalent in AML, is so far unclear and needs to be carefully evaluated in future trials. Because preclinical data indicate that this class of drugs has the ability to eradicate acute leukemia, even as a monotherapy, it will be important to identify markers that can predict incomplete responses with the goal of starting combination therapies at an early point. Which Menin–UTX targets may serve as good biomarkers with sufficient sensitivity and specificity remains to be investigated in more upcoming clinical trials.

METHODS

Plasmids and sgRNA Cloning

To generate stable Cas9-expressing cell lines, we used lentiCas9-Blast (Addgene, 52962). Human wild-type or mutant (K4M) histone H3.1 were cloned into pCDH-EF1-MCS-IRES-RFP (System Biosciences, CD531A-2). To express sgRNAs, we generated the pUSEPR (U6-sgRNA-EFS-Puro-P2A-TurboRFP) and pUSEPB (U6-sgRNA-EFS-Puro-P2A-TagBFP) lentiviral vectors by Gibson assembly of the following DNA fragments: (i) PCR-amplified U6-sgRNA (improved scaffold; ref. 95) cassette, (ii) PCR-amplified EF1s promoter, (iii) PCR-amplified Puro-P2A-TurboRFP (or -TagBFP) gene fragment (IDT), and (iv) BsrGI/PmeI-digested pLL3-based lentiviral backbone (96). For sgRNA cloning, pUSEPR and pUSEPB vectors were linearized with BsmBI (NEB) and ligated with BsmBI-compatible annealed and phosphorylated oligos encoding sgRNAs using high-concentration T4 DNA ligase (NEB). All sgRNA sequences used are listed in Supplementary Table S1.

Cell Culture

Mouse MLL-AF9 leukemia cells were kindly shared by David Chen (Chun-Wei Chen, City of Hope) and were originally generated by the transformation of female mouse bone marrow Lin-Sca1$^+$cKit$^+$ (LSK) cells with an MSCV-IRES-GFP (pMIG) retrovirus expressing the human MLL–AF9 fusion protein and transplanted into sublethally irradiated recipient mice as described previously (29, 47). Leukemic blasts were harvested from moribund mice and cultured *in vitro* in IMDM (Gibco) supplemented with 15% FBS (Gibco), mouse IL6 (10 ng/μL, PeproTech), mouse IL3 (10 ng/μL, PeproTech), mouse SCF (20 ng/μL, PeproTech), penicillin (100 U/mL, Gibco), streptomycin (100 μg/μL, Gibco), L-glutamine (2 mmol/L, Gibco), and plasmocin (5 μg/mL, InvivoGen). Human leukemia cell lines MV4;11 and OCI-AML3 were kindly shared by Zhaohui Feng (Dana-Farber Cancer Institute) and were cultured in RPMI 1640 (Corning) supplemented with 10% FBS (Gibco), penicillin (100 U/mL, Gibco), streptomycin (100 μg/μL, Gibco), L-glutamine (2 mmol/L, Gibco), and plasmocin (5 μg/mL, InvivoGen). Mouse NIH-3T3 cells were maintained in DMEM (Corning) supplemented with 10% FCS (ATCC), penicillin (100 U/mL, Gibco), streptomycin (100 μg/μL, Gibco), and plasmocin (5 μg/mL, InvivoGen). Human HEK293 cells were maintained in DMEM (Corning) supplemented with 10% FBS (Gibco), penicillin (100 U/mL, Gibco), streptomycin (100 μg/μL, Gibco), and plasmocin (5μg/mL, InvivoGen). Cas9-expressing cells were generated by lentiviral transduction of lentiCas9-Blast, followed by blasticidin (InvivoGen) selection and validation of Cas9 expression and activity. All cells were confirmed to be free of *Mycoplasma* contamination and cultured at 37°C and 5% CO_2.

Virus Production

Lentiviruses were produced by the cotransfection of HEK293T (ATCC) cells with pUSEPR-EpiV2.0 sgRNA library, individual sgRNA plasmids, or lentiCas9-Blast, and packaging vectors psPax2 (Addgene, 12260) and pMD2.G (Addgene, 12259) using Lipofectamine 2000 (Invitrogen). Viral supernatants were collected at 48 and 72 hours after transfection and stored at −80°C.

Transduction of Cell Lines

Leukemia cells were seeded at a density of 2.5×10^5 cells/well of a non–tissue culture-treated, 12-well plate in complete medium containing polybrene (10 μg/mL, EMD Millipore) and then transduced with lentivirus by centrifugation at 2,500 rpm for 90 minutes at 37°C. After a 24-hour incubation, cells were transferred to a new plate containing fresh culture medium. Antibiotic selection or cell sorting was done 48 hours after transduction.

Drug Treatments

For MI-503 (Active Biochem) treatments, leukemia cells were seeded at a density of 4×10^5 cells/mL and treated with limiting dilutions of the inhibitor as indicated or 0.25% DMSO (vehicle). Cells were replated every 4 days to the initial density and retreated. Viability was assessed at various time points by using the CellTiter-Glo Luminescent Cell Viability assay (Promega) following the manufacturer's guidelines. The ratio of luminescence signal from metabolically active cells in MI-503 versus DMSO was plotted to calculate IC_{50} (concentration of a drug that inhibits growth by 50%) values (Prism 8, GraphPad). For MI-503 (Active Biochem) and palbociclib HCl (Selleckchem) combination treatments, 25,000 leukemia cells in 250 μL of drug-containing medium were seeded in a 48-well plate, and viability was assessed every 4 days using the CellTiter-Glo Luminescent Cell Viability assay (Promega). For RNA-seq and ChIP-seq experiments, cells were cultured at 4×10^5 cells/mL and treated with MI-503 (concentrations as indicated in figure legends) or 0.25% DMSO for 4 days. Cells were collected, washed with PBS, pelleted, and flash-frozen before RNA or chromatin isolation. For *in vivo* VTP-50649 treatment, mice were randomly assigned to either normal or 0.1% VTP-50469 rodent special diet. Mice were bled weekly to monitor leukemia burden and euthanized when they showed clinical signs of disease (experimental endpoint).

Flow Cytometric Analyses

Immunophenotyping of leukemia cells treated with MI-503 (or vehicle) was done by collecting cells after treatment and staining them using the indicated conjugated primary antibodies. Stained samples were analyzed on an LSRFortessa (BD Biosciences) flow cytometer. Data analysis was performed using FlowJo (BD Biosciences) software. Intracellular antigen detection was done using the Foxp3/Transcription Factor Staining Buffer Set (eBioscience) following the manufacturer's guidelines. Conjugated primary antibodies used were Pacific Blue anti-CD11b (BioLegend, 101224) and Alexa Fluor 647 anti-Cas9 (Cell Signaling Technology, 48796).

Xenograft Models of AML

All animal experiments were performed with the approval of Dana-Farber Cancer Institute's Institutional Animal Care and Use Committee. NOD.Cg-*Prkdc*^{scid} *Il2rg*^{tm1Sug}/JicTac (NOG) mice were obtained from Taconic Biosciences. Nonirradiated 8- to 12-week-old adult mice were transplanted with previously established PDXs (25) via tail-vein injection (250,000 cells/mouse). Engraftment of human cells (hCD45$^+$) was analyzed and monitored longitudinally by weekly

bleeding to quantify hCD45$^+$ cells in the peripheral blood by flow cytometry with human CD45-PE and anti-mouse CD45-APC-Cy7 antibodies (BioLegend). Mice were monitored closely to detect disease onset, and treatment started when hCD45$^+$ cells were detectable in the peripheral blood. Mice were randomly assigned to either normal or 0.1% VTP-50469 rodent special diet (25). Mice were bled weekly to monitor leukemia burden as described above and euthanized when showing clinical signs of disease (experimental endpoint). Leukemia cells from a subset of these animals were harvested after 7 days of treatment to perform RNA-seq.

Longitudinal Analysis of AML Patients Treated with SNDX-5613

Peripheral blood was taken under written informed consent from patients during routine blood draws at screening and different timepoints during the first cycle of treatment with SDNX-5613 within the AUGMENT-101 clinical trial (NCT04065399). These studies were conducted in accordance with the Declaration of Helsinki and were approved by an institutional review board (IRB) at the Dana-Farber Cancer Institute (IRB: #01-206). Peripheral blood mononuclear cells were subsequently isolated using Ficoll (BD Biosciences) gradient centrifugation, viably frozen, and banked at the Dana-Farber Cancer Institute. For longitudinal analysis, samples were thawed, washed twice in PBS, and stained with anti-human CD45 (PE; BioLegend, 304007) and anti-human CD117 (APC; BioLegend, 313205). CD45^{lo}/CD117$^+$ leukemia cells were FACS-sorted (Sony MA900 sorter) and subsequently processed for RNA-seq (see Methods section on RNA-seq).

Immunoblotting

Whole-cell lysates were separated by SDS-PAGE, transferred to a PVDF membrane (EMD Millipore), blocked in 5% nonfat milk in TBS plus 0.5% Tween-20 (Sigma-Aldrich), probed with primary antibodies, and detected with HRP-conjugated anti-rabbit or anti-mouse secondary antibodies (GE Healthcare). Primary antibodies used included anti-Cas9 (Cell Signaling Technology, 14697), anti-UTX (Cell Signaling Technology, 33510), anti-Menin (Bethyl, A300-105A), anti-NF-YA (Santa Cruz Biotechnology, sc-17753), anti-Actin (Abcam, ab8224), anti-HSP90 (BD Biosciences, 610418), anti-HA (BioLegend, 901501), anti-H3K4me1 (Abcam, ab8895), anti-H3K4me3 (Cell Signaling Technology, 9751), and anti-H3 (Abcam, ab1791).

Locus-Specific DNA Sequencing

To determine the mutational status of the *Men1* and *Utx* loci in cells targeted by CRISPR–Cas9, we performed next-generation sequencing of PCR-amplified target regions. Genomic DNA (gDNA) was isolated using the DNeasy Blood and Tissue Kit (Qiagen) following the manufacturer's guidelines. Amplification of target regions was performed from 500 ng of gDNA using Q5 High-Fidelity 2X Master Mix (NEB) and primers listed in Supplementary Table S1. PCR products were purified using the QIAquick PCR Purification Kit (Qiagen) and sequenced on Illumina instruments at GENEWIZ (Amplicon-EZ service).

RNA Isolation, qPCR Analyses, and RNA-seq

Total RNA was isolated from cells using the RNeasy kit (Qiagen). RNA was reverse transcribed with High-Capacity cDNA Reverse Transcription kits (Applied Biosystems) following the manufacturer's instructions. Quantitative PCRs (qPCRs) were performed using the TaqMan Gene Expression Master Mix (Applied Biosystems) with the StepOne Real-Time System (Applied Biosystems). TaqMan gene expression assays were used. *ActB* was used as the endogenous control for normalization, and relative gene expression was calculated by using the comparative C_T method. The mouse gene probes used were *ActB* (Mm02619580_g1), *Hoxa9* (Mm00439364_m1), *Meis1* (Mm00487664_m1), *Utx* (*Kdm6a*) (Mm00801998_m1), and *Men1* (Mm00484957_m1). The quality of extracted RNA for sequencing was assessed by RIN using a Bioanalyzer (Agilent) and quantified by TapeStation (Agilent). Poly(A) mRNA enrichment and library preparation were performed using the NEBNext Poly(A) mRNA Magnetic Isolation Module and NEBNext Ultra II RNA Library Prep kit (NEB). Sequencing was done using the Illumina NextSeq 500 to obtain >20 million 75-bp, single-end or 37-bp, paired-end reads per sample (HiSeq 2500, 150 bp, paired-end; Illumina).

Cloning of sgRNA Library Targeting Mouse Chromatin Regulators

sgRNA sequences (six per gene) targeting 616 mouse chromatin regulators (for a total of 3,696 sgRNAs; Supplementary Table S1) were designed using the Broad Institute sgRNA Designer tool (97). We also included 36 nontargeting control sgRNAs obtained from the GeCKOv2 Mouse CRISPR library (refs. 98; for a total of 3,732 sgRNAs). This library was divided into 6 pools (each composed of 616 targeting and 6 nontargeting sgRNAs), synthesized by Agilent Technologies, and cloned into the pUSEPR lentiviral vector (99) using a modified version of the protocol published by Doench and colleagues (97) to ensure a library representation of >10,000×. Briefly, each subpool was selectively amplified using barcoded forward and reverse primers that append cloning adapters at the 5′- and 3′-ends of the sgRNA insert (Supplementary Table S1), purified using the QIAquick PCR Purification Kit (Qiagen), and ligated into BsmBI-digested and dephosphorylated pUSEPR vector using high-concentration T4 DNA ligase (NEB). A minimum of 1.2 μg of ligated pUSEPR plasmid DNA per subpool was electroporated into Endura electrocompetent cells (Lucigen), recovered for 1 hour at 37°C, plated across four 15-cm LB-Carbenicillin plates (Teknova), and incubated at 37°C for 16 hours. The total number of bacterial colonies per subpool was quantified using serial dilution plates to ensure a library representation of >10,000 × (>6.2 million colonies per subpool). The next morning, bacterial colonies were scraped and briefly expanded for 4 hours at 37°C in 500 mL of LB-carbenicillin. Plasmid DNA was isolated using the Plasmid Plus Maxi Kit (Qiagen).

To assess sgRNA distribution in each of the subpools, as well as the master pool (composed of equimolar amounts of plasmid DNA from each individual subpool), we amplified the sgRNA target region using primers that append Illumina sequencing adapters on the 5′- and 3′-ends of the amplicon, as well as a random nucleotide stagger and unique demultiplexing barcode on the 5′-end (Supplementary Table S1). Library amplicons were size-selected on a 2.5% agarose gel, purified using the QIAquick Gel Extraction Kit (Qiagen), and sequenced on an Illumina NextSeq instrument (75-nt, single-end reads).

Chromatin-Focused CRISPR–Cas9 Genetic Screening

To ensure that most cells harbor a single sgRNA integration event, we determined the volume of viral supernatant that would achieve a multiplicity of infection (MOI) of ~0.3 upon spin infection of a population of Cas9-expressing leukemia cells. Briefly, cells were plated at a concentration of 2.5×10^5 per well in 12-well plates along with increasing volumes of master pool viral supernatant (0, 25, 100, 200, 500, 1,000, and 2,000 μL) and polybrene (10 μg/mL, EMD Millipore). Cells were then centrifuged at 1,500 rpm for 2 hours at 37°C and incubated at 37°C overnight. Viral infection efficiency was determined by the percentage of tRFP$^+$ cells assessed by flow cytometry on an LSRFortessa (BD Biosciences) instrument 72 hours after infection.

Each step of the screen—from infection to sequencing—was optimized to achieve a minimum representation of 1,000×. To ensure a representation of 1,000× at the transduction step, we spin-infected a total of 20 million cells across seven 12-well plates in triplicate (for a

total of 21 12-well plates) using the volume of viral supernatant that would achieve a 30% infection rate (6 million transduced cells per technical replicate).

Twenty-four hours after infection, cells were pooled into 2 × T-225 flasks (Corning) per infection replicate and selected with 2.5 μg/mL puromycin (Gibco) for 4 days. Subsequently, 6 million puromycin-selected cells were pelleted and stored at −20°C (T_0/input population), whereas the rest were plated into either DMSO- or MI-503–containing media (at an IC_{50} concentration) and cultured until the population reached 12 cumulative population doublings (T_F/final). At least 6 million cells were harvested and pelleted for this final time point. gDNA from MLL-AF9 cells was isolated using the DNeasy Blood and Tissue Kit (Qiagen) following the manufacturer's guidelines.

We assumed that each cell contained approximately 6.6 pg of gDNA, as previously published (100). Therefore, deconvolution of the screen at 1,000× required sampling ~4 million × 6.6 pg of gDNA, or ~26.4 μg. We used a modified two-step PCR version of the protocol published by Doench and colleagues (97). Briefly, we performed an initial "enrichment" PCR, whereby the integrated sgRNA cassettes were amplified from gDNA, followed by a second PCR to append Illumina sequencing adapters on the 5′- and 3′-ends of the amplicon, as well as a random nucleotide stagger and unique demultiplexing barcode on the 5′-end. Each "PCR1" reaction contains 25 μL of Q5 High-Fidelity 2X Master Mix (NEB), 2.5 μL of Nuc PCR#1 Fwd Primer (10 μm), 2.5 μL of Nuc PCR#1 Rev Primer (10 μmol/L), and 5 μg of gDNA in 20 μL of water (for a total volume of 50 μL per reaction). The number of PCR1 reactions is scaled accordingly; therefore, we performed six PCR1 reactions per technical replicate, per time point (T_0 or T_F), and per condition (DMSO or MI-503). PCR1 amplicons were purified using the QIAquick PCR Purification Kit (Qiagen) and used as a template for "PCR2" reactions. Each PCR2 reaction contains 25 μL of Q5 High-Fidelity 2X Master Mix (NEB), 2.5 μL of a unique Nuc PCR#2 Fwd Primer (10 μmol/L), 2.5 μL of Nuc PCR#2 Rev Primer (10 μmol/L), and 300 ng of PCR1 product in 20 μL of water (for a total volume of 50 μL per reaction). We performed two PCR2 reactions per PCR1 product. Library amplicons were size-selected on a 2.5% agarose gel, purified using the QIAquick Gel Extraction Kit (Qiagen), and sequenced on an Illumina NextSeq 500 instrument (75-nt, single-end reads). All primer sequences are available in Supplementary Table S1. The PCR conditions used for PCR1 and PCR2 were as follows: (i) 98°C for 30 seconds; (ii) 98°C for 10 seconds; (iii) 65°C for 30 seconds; (iv) 72°C for 30 seconds; (v) steps ii to iv repeated for 24 cycles; (vi) 72°C for 2 minutes; and (vii) 4°C forever.

Genome-wide CRISPR–Cas9 Genetic Screening

Paired mouse genome-scale CRISPR–Cas9 screening libraries (M1/M2) were used (Addgene Pooled Library #1000000173). The M1 and M2 libraries cover protein-coding genes of the genome with a total of 10 guide RNAs per gene. Lentivirus was produced using each separate library pool and used to transduce each 5 × 10^8 MLL-AF9 cells at low MOI. Forty-eight hours after library transduction, cells were selected with blasticidin (5 μg/mL). After 5 days of antibiotic selection, a baseline (T_0) sample was collected, and cells were cultured in duplicate before the harvest of terminal samples after 12 days (T_F). Subsequently, gDNA was isolated using phenol-chloroform extraction, and sgRNA libraries were deconvoluted using next-generation sequencing essentially as described above.

Analysis of CRISPR–Cas9 Genetic Screen Data

FASTQ files were processed and trimmed to retrieve sgRNA target sequences followed by alignment to the reference sgRNA library file. Sequencing read counts were summarized at the gene level per sample and used as input to run differential analysis using the DESeq2 package. The $\log_2$ fold-change values were used as "Gene Score" for the final visualization. Genome-wide screening data were analyzed using MAGeCK MLE essentially as described in the original publication (101). See Supplementary Table S2 for all raw screening data.

Growth Competition Assays

Cas9-expressing cells were virally transduced with the designated constructs (pUSEPR-sgRNA, pUSEPB-sgRNA, pCDH-cDNA) in 12-well plates at 30% to 40% infection rate (three infection replicates). Cells were monitored by flow cytometry over time using an LSRFortessa (BD Biosciences) flow cytometer, and relative growth of sgRNA-containing cells was assessed. Flow cytometry data were analyzed with FlowJo software (BD Biosciences). The percentage of single-positive (tRFP$^+$ or BFP$^+$) or double-positive (tRFP$^+$/BFP$^+$) cells was normalized to their respective "T_0" time-point values (assessed on day 2 or 3 after transduction, as indicated in the figure legend). Normalized values were $\log_2$-transformed, and the relative cell proliferation was calculated as follows:

$$\text{Relative cell proliferation} = \log_2(\text{normalized DP}) - \log_2(\text{normalized SP})$$

ChIP

Cross-linking ChIP in mouse leukemia and NIH-3T3 cells was performed with 10 × 10^7 to 20 × 10^7 cells per immunoprecipitation. After drug (or vehicle) treatment, cells were collected, washed once with ice-cold PBS, and flash-frozen. Cells were resuspended in ice-cold PBS and cross-linked using 1% paraformaldehyde (PFA; Electron Microscopy Sciences) for 5 minutes at room temperature with gentle rotation. Unreacted PFA was quenched with glycine (final concentration 125 mmol/L) for 5 minutes at room temperature with gentle rotation. Cells were washed once with ice-cold PBS and pelleted by centrifugation (800 × *g* for 5 minutes). To obtain a soluble chromatin extract, cells were resuspended in 1 mL of LB1 (50 mmol/L HEPES pH 7.5, 140 mmol/L NaCl, 1 mmol/L EDTA, 10% glycerol, 0.5% NP-40, 0.25% Triton X-100, and 1× complete protease inhibitor cocktail) and incubated at 4°C for 10 minutes while rotating. Samples were centrifuged (1,400 × *g* for 5 minutes), resuspended in 1 mL of LB2 (10 mmol/L Tris-HCl pH 8.0, 200 mmol/L NaCl, 1 mmol/L EDTA, 0.5 mmol/L EGTA, and 1× complete protease inhibitor cocktail), and incubated at 4°C for 10 minutes while rotating. Finally, samples were centrifuged (1,400 × *g* for 5 minutes) and resuspended in 1 mL of LB3 (10 mmol/L Tris-HCl pH 8.0, 100 mmol/L NaCl, 1 mmol/L EDTA, 0.5 mmol/L EGTA, 0.1% sodium deoxycholate, 0.5% N-Lauroylsarcosine, and 1× complete protease inhibitor cocktail). Samples were homogenized by passing 7 to 8 times through a 28-gauge needle, and Triton X-100 was added to a final concentration of 1%. Chromatin extracts were sonicated for 14 minutes using a Covaris E220-focused ultrasonicator. Lysates were centrifuged at maximum speed for 10 minutes at 4°C, and 5% of supernatant was saved as input DNA. Beads were prepared by incubating them in 0.5% BSA in PBS and antibodies overnight [100 μL of Dynabeads Protein A or Protein G (Invitrogen) plus 20 μL of antibody]. Antibodies used were anti-Menin (Bethyl, A300-105A), anti-UTX (Bethyl, A302-374A), anti-MLL1 (N-term-specific, Bethyl, A300-086A), anti-MLL3/4 (kindly provided by the Wysocka Laboratory; ref. 38), anti–NF-YA (Santa Cruz Biotechnology, sc-17753), anti-H3K4me1 (Abcam, ab8895), anti-H3K4me3 (Active Motif, 39159), and anti-H4K16ac (Active Motif, 39167). Antibody–bead mixes were washed with 0.5% BSA in PBS and then added to the lysates overnight while rotating at 4°C. Beads were then washed six times with RIPA buffer (50 mmol/L HEPES pH 7.5, 500 mmol/L LiCl, 1 mmol/L EDTA, 0.7% sodium deoxycholate, and 1% NP-40) and once with TE-NaCl buffer (10 mmol/L Tris-HCl pH 8.0, 50 mmol/L NaCl, and 1 mmol/L EDTA). Chromatin was eluted from beads in elution buffer (50 mmol/L Tris-HCl pH 8.0, 10 mmol/L EDTA, and 1% SDS)

by incubating at 65°C for 30 minutes while shaking, supernatant was removed by centrifugation, and cross-linking was reversed by further incubating chromatin overnight at 65°C. The eluted chromatin was then treated with RNaseA (10 mg/mL) for 1 hour at 37°C and with Proteinase K (Roche) for 2 hours at 55°C. DNA was purified by using phenol-chloroform extraction followed with ethanol precipitation. The NEBNext Ultra II DNA Library Prep kit was used to prepare samples for sequencing on an Illumina NextSeq 500 (75-bp read length, single-end, or 37-bp read length, paired-end).

ChIP-seq Analysis

ChIP-sequencing samples were sequenced using the Illumina NextSeq500. ChIP-seq reads were aligned using Rsubread's align method, and predicted fragment lengths were calculated by the ChIPQC R Bioconductor package (102, 103). Normalized, fragment-extended signal bigWigs were created using the rtracklayer R Bioconductor package. Peak calls were made in MACS2 software (104). Read counts in peaks were calculated using the featureCounts method in the Rsubread library (103). Differential ChIP-seq signals were identified using the binomTest from the edgeR R Bioconductor package (105). Annotation of genomic regions to genes, biological functions, and pathways was performed using the ChIPseeker R Bioconductor package (106). Meta-peak plots were produced using the soGGi package, and ChIP-seq signal heat maps were generated using the deepTools and profileplyr software (107). Plots showing ChIP-seq read signal over TSSs were made with the ngs.plot software package (v2.61; ref. 108). Overlaps between peak sets were determined using the ChIPpeakAnno R Bioconductor package with a maximum gap between peaks set to 1 kb (109). Peaks were annotated with both genes and the various types of genomic regions using the ChIPseeker R Bioconductor package (106). Range-based heat maps showing signal over genomic regions were generated using the soGGi and profileplyr R Bioconductor package to quantify read signal and group the peak ranges and the deepTools software package (v3.3.1) to generate the heat maps (107). Any regions included in the ENCODE blacklisted regions of the genome were excluded from all region-specific analyses (110). For some ChIP-seq experiments, raw Illumina NextSeq BCL files were converted to FASTQs using Illumina bcl2fastq v02.14.01.07, and reads were trimmed using Trimmomatic v0.36 (phred quality threshold 33) and uploaded to the Basepair-server (basepairtech.com). Alignment and ChIP-seq quality control was performed on the basepair platform (Bowtie2). Peak calling was performed using MACS (v.1.4) within the basepair platform utilizing the default parameters.

RNA-seq Analysis

RNA-seq samples were sequenced using the Illumina NextSeq500 instrument. Transcript abundance was computed from FASTQ files using Salmon and the GENCODE reference transcript sequences, transcript counts were imported into R with the tximport R Bioconductor package, and differential gene expression was determined with the DESeq2 R Bioconductor package (111–113). The data were visualized using the ggplot2 R package. Normalized counts were extracted from the DESeq2 results and *z*-scores for the indicated gene sets were visualized using both heat maps and box plots. Heat maps showing gene expression changes across samples were generated using the pheatmap R package, and box plots were made with the ggplot2 R package. Gene ontology analysis using the Kyoto Encyclopedia of Genes and Genomes (KEGG) 2019 database was performed using the *Enrichr* tool (65).

Statistical Analyses

Statistical tests were used as indicated in the figure legends. Generation of plots and statistical analyses were performed using Prism 8 (GraphPad). Error bars represent standard deviation unless otherwise noted. We used Student *t* test (unpaired, two-tailed) to assess the significance between treatment and control groups, and to calculate *P* values. $P < 0.05$ was considered statistically significant.

Source Data Availability

Data supporting the findings of this study are reported in Supplementary Figures S1–S25 and Supplementary Tables S1–S4. All raw data corresponding to high-throughput approaches (CRISPR screens, RNA-seq, and ChIP-seq) are available through the NCBI's Gene Expression Omnibus (GSE186711). All reagents and materials generated in this study will be available to the scientific community through Addgene and/or material transfer agreements. Further information and requests for resources and reagents should be directed to and will be fulfilled by the corresponding authors: C. David Allis (alliscd@rockefeller.edu), Scott W. Lowe (lowes@mskcc.org), and Scott. A. Armstrong (Scott_A rmstrong@dfci.harvard.edu).

Authors' Disclosures

Y.M. Soto-Feliciano reports grants from the Damon Runyon Foundation and the NIH/National Institute of General Medical Sciences during the conduct of the study, as well as consulting fees from Scaffold Tx outside the submitted work. E.R. Kastenhuber reports current employment at Loxo Oncology at Eli Lilly. S. Gu reports grants from the Sara Elizabeth O'Brien Trust Fellowship during the conduct of the study. X.S. Liu reports grants from the NIH during the conduct of the study; grants from Sanofi, Takeda, Novartis, and the Breast Cancer Research Foundation outside the submitted work; and conducted this work while a faculty member of Dana-Farber Cancer Institute and is currently a board member for and CEO of GV20 Therapeutics. R.M. Stone reports personal fees from AbbVie, AbbVie/Genentech, Actinium, Aprea, Aptevo, Arog, AvenCell, BerGenBio, Boston Pharmaceuticals, Bristol Myers Squibb, CTI Pharma, Elevate Bio, Foghorn, GeMoab, GSK, Innate, Jazz, Janssen, Kura Oncology, Epizyme, OncoNova, Syntrix/ACI, Syros, Syndax, Novartis, and Takeda outside the submitted work. S.A. Armstrong reports grants from the NCI during the conduct of the study; grants and nonfinancial support from Syndax, personal fees from C4 Therapeutics, Imago Biosciences, Accent Therapeutics, Cyteir Therapeutics, Mana Therapeutics, and Neomorph Therapeutics, and grants from Janssen outside the submitted work; and a patent for MENIN inhibition (WO/2017/132398A1) issued, licensed, and with royalties paid. S.W. Lowe reports consulting for and equity in Oric Pharmaceuticals, Blueprint Medicines, Mirimus, Senecea Therapeutics, Faeth Therapeutics, and PMV Pharmaceuticals not directly related to this manuscript. C.D. Allis reports grants from The Leukemia & Lymphoma Society, the NIH/NCI, the NIH/National Institute of General Medical Sciences, and St. Jude Children's Research Hospital during the conduct of the study, as well as other support from Chroma Therapeutics, Constellation Pharmaceuticals, and EpiCypher outside the submitted work. No disclosures were reported by the other authors.

Authors' Contributions

Y.M. Soto-Feliciano: Conceptualization, resources, data curation, formal analysis, validation, investigation, visualization, methodology, writing–original draft, project administration, writing–review and editing. **F.J. Sanchez-Rivera:** Conceptualization, data curation, formal analysis, investigation, visualization, methodology, writing–original draft, writing–review and editing. **F. Perner:** Resources, data curation, formal analysis, validation, investigation, writing–review and editing. **D.W. Barrows:** Data curation, software, formal analysis, visualization, methodology. **E.R. Kastenhuber:** Data curation, formal analysis, visualization, methodology. **Y.-J. Ho:** Data curation, formal analysis, visualization. **T. Carroll:** Data curation, software, formal analysis, visualization. **Y. Xiong:** Investigation. **D. Anand:** Investigation. **A.A. Soshnev:** Visualization, methodology.

L. Gates: Validation, investigation, methodology. **M.C. Beytagh:** Investigation. **D. Cheon:** Validation, investigation. **S. Gu:** Investigation. **X.S. Liu:** Resources. **A.V. Krivtsov:** Resources. **M. Meneses:** Resources. **E. de Stanchina:** Resources. **R.M. Stone:** Resources. **S.A. Armstrong:** Resources, supervision, funding acquisition, writing–review and editing. **S.W. Lowe:** Conceptualization, supervision, funding acquisition, writing–original draft, project administration, writing–review and editing. **C.D. Allis:** Conceptualization, resources, supervision, funding acquisition, writing–original draft, project administration, writing–review and editing.

Acknowledgments

We thank members of the Allis, Lowe, and Armstrong laboratories for their help and support; Richard Phillips, Robert G. Roeder, Tom W. Muir, Benjamin A. Garcia, and Charles J. Sherr for scientific discussions; David Chen (Chun-Wei Chen) for mouse MLL-AF9 cells, Zhaohui Feng for human leukemia cells, and Laura Whitman (Agilent) for oligonucleotide synthesis support. C.D. Allis was supported by NIH grants (P01CA196539 and 5R01CA204639), The Leukemia & Lymphoma Society (LLS-SCOR 7006-13), and The Rockefeller University and St. Jude Children's Research Hospital Collaborative on Chromatin Regulation in Pediatric Cancer. S.W. Lowe was supported by an NIH/NCI grant (R01CA190261) and an Agilent Thought Leader Award, as well as the Memorial Sloan Kettering Cancer Center cancer center support grant (P30CA008748). S.W. Lowe is the Geoffrey Beene Chair of Cancer Biology and a Howard Hughes Medical Institute Investigator. S.A. Armstrong was supported by NIH grants CA176745, CA206963, CA204639, and CA066996. Y.M. Soto-Feliciano was supported by the Damon Runyon-Sohn Pediatric Cancer Fellowship (DRSG-21-17) and a National Institute of General Medical Sciences Maximizing Opportunities for Scientific and Academic Independent Careers (NIGMS-MOSAIC) K99/R00 Career Development Award (1K99GM140265). F.J. Sanchez-Rivera was partially supported by the MSKCC TROT program (5T32CA160001) and a Memorial Sloan Kettering Cancer Center GMTEC Postdoctoral Researcher Innovation Grant and is a Howard Hughes Medical Institute Hanna Gray Fellow. F. Perner was supported by a postdoctoral fellowship of the German Research Foundation (DFG, PE 3217/1-1), a grant from Else Kröner-Fresenius Stiftung (EKFS; 2021_EKEA.111), and a Momentum Fellowship award by the Mark Foundation for Cancer Research. D.W. Barrows was supported by a Ruth L. Kirschstein National Research Service Award (5F32CA217068). E.R. Kastenhuber was supported by an F31 National Research Service Award predoctoral fellowship from the NIH/NCI (F31CA192835).

The publication costs of this article were defrayed in part by the payment of publication fees. Therefore, and solely to indicate this fact, this article is hereby marked "advertisement" in accordance with 18 USC section 1734.

Note

Supplementary data for this article are available at Cancer Discovery Online (http://cancerdiscovery.aacrjournals.org/).

Received April 13, 2022; revised August 18, 2022; accepted October 17, 2022; published first October 20, 2022.

REFERENCES

1. Guru SC, Goldsmith PK, Burns AL, Marx SJ, Spiegel AM, Collins FS, et al. Menin, the product of the MEN1 gene, is a nuclear protein. Proc Natl Acad Sci U S A 1998;95:1630–4.
2. Hughes CM, Rozenblatt-Rosen O, Milne TA, Copeland TD, Levine SS, Lee JC, et al. Menin associates with a trithorax family histone methyltransferase complex and with the hoxc8 locus. Mol Cell 2004;13:587–97.
3. Milne TA, Hughes CM, Lloyd R, Yang Z, Rozenblatt-Rosen O, Dou Y, et al. Menin and MLL cooperatively regulate expression of cyclin-dependent kinase inhibitors. Proc Natl Acad Sci U S A 2005;102:749–54.
4. Yokoyama A, Somervaille TCP, Smith KS, Rozenblatt-Rosen O, Meyerson M, Cleary ML. The menin tumor suppressor protein is an essential oncogenic cofactor for MLL-associated leukemogenesis. Cell 2005;123:207–18.
5. Brès V, Yoshida T, Pickle L, Jones KA. SKIP interacts with c-Myc and Menin to promote HIV-1 Tat transactivation. Mol Cell 2009;36:75–87.
6. Agarwal SK, Jothi R. Genome-wide characterization of menin-dependent H3K4me3 reveals a specific role for menin in the regulation of genes implicated in MEN1-like tumors. PLoS One 2012;7:e37952.
7. Huang J, Gurung B, Wan B, Matkar S, Veniaminova NA, Wan K, et al. The same pocket in menin binds both MLL and JUND but has opposite effects on transcription. Nature 2012;482:542–6.
8. Kaji H, Canaff L, Lebrun JJ, Goltzman D, Hendy GN. Inactivation of menin, a Smad3-interacting protein, blocks transforming growth factor type beta signaling. Proc Natl Acad Sci U S A 2001;98:3837–42.
9. Sowa H, Kaji H, Canaff L, Hendy GN, Tsukamoto T, Yamaguchi T, et al. Inactivation of menin, the product of the multiple endocrine neoplasia type 1 gene, inhibits the commitment of multipotential mesenchymal stem cells into the osteoblast lineage. J Biol Chem 2003;278:21058–69.
10. Yokoyama A, Cleary ML. Menin critically links MLL proteins with LEDGF on cancer-associated target genes. Cancer Cell 2008;14:36–46.
11. Balogh K, Rácz K, Patócs A, Hunyady L. Menin and its interacting proteins: elucidation of menin function. Trends Endocrinol Metab 2006;17:357–64.
12. Yokoyama A, Wang Z, Wysocka J, Sanyal M, Aufiero DJ, Kitabayashi I, et al. Leukemia proto-oncoprotein MLL forms a SET1-like histone methyltransferase complex with menin to regulate Hox gene expression. Mol Cell Biol 2004;24:5639–49.
13. Wang P, Lin C, Smith ER, Guo H, Sanderson BW, Wu M, et al. Global analysis of H3K4 methylation defines MLL family member targets and points to a role for MLL1-mediated H3K4 methylation in the regulation of transcriptional initiation by RNA polymerase II. Mol Cell Biol 2009;29:6074–85.
14. Chandrasekharappa SC, Guru SC, Manickam P, Olufemi SE, Collins FS, Emmert-Buck MR, et al. Positional cloning of the gene for multiple endocrine neoplasia-type 1. Science 1997;276:404–7.
15. Jiao Y, Shi C, Edil BH, de Wilde RF, Klimstra DS, Maitra A, et al. DAXX/ATRX, MEN1, and mTOR pathway genes are frequently altered in pancreatic neuroendocrine tumors. Science 2011;331:1199–203.
16. Asgharian B, Turner ML, Gibril F, Entsuah LK, Serrano J, Jensen RT. Cutaneous tumors in patients with multiple endocrine neoplasm type 1 (MEN1) and gastrinomas: prospective study of frequency and development of criteria with high sensitivity and specificity for MEN1. J Clin Endocrinol Metab 2004;89:5328–36.
17. Pei XH, Bai F, Smith MD, Xiong Y. p18Ink4c collaborates with Men1 to constrain lung stem cell expansion and suppress non-small-cell lung cancers. Cancer Res 2007;67:3162–70.
18. Falchetti A, Marini F, Luzi E, Giusti F, Cavalli L, Cavalli T, et al. Multiple endocrine neoplasia type 1 (MEN1): not only inherited endocrine tumors. Genet Med 2009;11:825–35.
19. Xu B, Li SH, Zheng R, Gao SB, Ding LH, Yin ZY, et al. Menin promotes hepatocellular carcinogenesis and epigenetically up-regulates Yap1 transcription. Proc Natl Acad Sci U S A 2013;110:17480–5.
20. Krivtsov AV, Armstrong SA. MLL translocations, histone modifications and leukaemia stem-cell development. Nat Rev Cancer 2007;7:823–33.
21. Lemos MC, Thakker RV. Multiple endocrine neoplasia type 1 (MEN1): analysis of 1336 mutations reported in the first decade following identification of the gene. Hum Mutat 2008;29:22–32.
22. Borkin D, He S, Miao H, Kempinska K, Pollock J, Chase J, et al. Pharmacologic inhibition of the Menin-MLL interaction blocks progression of MLL leukemia in vivo. Cancer Cell 2015;27:589–602.

23. Dreijerink KMA, Groner AC, Vos ESM, Font-Tello A, Gu L, Chi D, et al. Enhancer-mediated oncogenic function of the menin tumor suppressor in breast cancer. Cell Rep 2017;18:2359–72.
24. Grembecka J, He S, Shi A, Purohit T, Muntean AG, Sorenson RJ, et al. Menin-MLL inhibitors reverse oncogenic activity of MLL fusion proteins in leukemia. Nat Chem Biol 2012;8:277–84.
25. Krivtsov AV, Evans K, Gadrey JY, Eschle BK, Hatton C, Uckelmann HJ, et al. A Menin-MLL inhibitor induces specific chromatin changes and eradicates disease in models of MLL-rearranged leukemia. Cancer Cell 2019;36:660–73.
26. Malik R, Khan AP, Asangani IA, Cieślik M, Prensner JR, Wang X, et al. Targeting the MLL complex in castration-resistant prostate cancer. Nat Med 2015;21:344–52.
27. Uckelmann HJ, Kim SM, Wong EM, Hatton C, Giovinazzo H, Gadrey JY, et al. Therapeutic targeting of preleukemia cells in a mouse model of NPM1 mutant acute myeloid leukemia. Science 2020;367:586–90.
28. Kurmasheva RT, Bandyopadhyay A, Favours E, Pozo VD, Ghilu S, Phelps DA, et al. Evaluation of VTP-50469, a Menin-MLL1 inhibitor, against Ewing sarcoma xenograft models by the pediatric preclinical testing consortium. Pediatr Blood Cancer 2020;67:e28284.
29. Chen CW, Koche RP, Sinha AU, Deshpande AJ, Zhu N, Eng R, et al. DOT1L inhibits SIRT1-mediated epigenetic silencing to maintain leukemic gene expression in MLL-rearranged leukemia. Nat Med 2015;21:335–43.
30. Bernt KM, Zhu N, Sinha AU, Vempati S, Faber J, Krivtsov AV, et al. MLL-rearranged leukemia is dependent on aberrant H3K79 methylation by DOT1L. Cancer Cell 2011;20:66–78.
31. Chang MJ, Wu H, Achille NJ, Reisenauer MR, Chou CW, Zeleznik-Le NJ, et al. Histone H3 lysine 79 methyltransferase Dot1 is required for immortalization by MLL oncogenes. Cancer Res 2010;70:10234–42.
32. Mueller D, García-Cuéllar M-P, Bach C, Buhl S, Maethner E, Slany RK. Misguided transcriptional elongation causes mixed lineage leukemia. PLoS Biol 2009;7:e1000249.
33. Zuber J, Shi J, Wang E, Rappaport AR, Herrmann H, Sison EA, et al. RNAi screen identifies Brd4 as a therapeutic target in acute myeloid leukaemia. Nature 2011;478:524–8.
34. Zuber J, Rappaport AR, Luo W, Wang E, Chen C, Vaseva AV, et al. An integrated approach to dissecting oncogene addiction implicates a Myb-coordinated self-renewal program as essential for leukemia maintenance. Genes Dev 2011;25:1628–40.
35. Meeks JJ, Shilatifard A. Multiple roles for the MLL/COMPASS family in the epigenetic regulation of gene expression and in cancer. Annu Rev Cancer Biol 2017;1:425–46.
36. Milne TA, Briggs SD, Brock HW, Martin ME, Gibbs D, Allis CD, et al. MLL targets SET domain methyltransferase activity to Hox gene promoters. Mol Cell 2002;10:1107–17.
37. Nakamura T, Mori T, Tada S, Krajewski W, Rozovskaia T, Wassell R, et al. ALL-1 is a histone methyltransferase that assembles a supercomplex of proteins involved in transcriptional regulation. Mol Cell 2002;10:1119–28.
38. Dorighi KM, Swigut T, Henriques T, Bhanu NV, Scruggs BS, Nady N, et al. Mll3 and Mll4 facilitate enhancer RNA synthesis and transcription from promoters independently of H3K4 monomethylation. Mol Cell 2017;66:568–76.
39. Herz HM, Mohan M, Garruss AS, Liang K, Takahashi Y-H, Mickey K, et al. Enhancer-associated H3K4 monomethylation by Trithorax-related, the Drosophila homolog of mammalian Mll3/Mll4. Genes Dev 2012;26:2604–20.
40. Hu D, Gao X, Morgan MA, Herz HM, Smith ER, Shilatifard A. The MLL3/MLL4 branches of the COMPASS family function as major histone H3K4 monomethylases at enhancers. Mol Cell Biol 2013;33:4745–54.
41. Lee J, Kim DH, Lee S, Yang QH, Lee DK, Lee SK, et al. A tumor suppressive coactivator complex of p53 containing ASC-2 and histone H3-lysine-4 methyltransferase MLL3 or its paralogue MLL4. Proc Natl Acad Sci U S A 2009;106:8513–8.
42. Wang SP, Tang Z, Chen CW, Shimada M, Koche RP, Wang LH, et al. A UTX-MLL4-p300 transcriptional regulatory network coordinately shapes active enhancer landscapes for eliciting transcription. Mol Cell 2017;67:308–21.
43. Santos MA, Faryabi RB, Ergen AV, Day AM, Malhowski A, Canela A, et al. DNA-damage-induced differentiation of leukaemic cells as an anti-cancer barrier. Nature 2014;514:107–11.
44. Gažová I, Lengeling A, Summers KM. Lysine demethylases KDM6A and UTY: the X and Y of histone demethylation. Mol Genet Metab 2019;127:31–44.
45. Kooistra SM, Helin K. Molecular mechanisms and potential functions of histone demethylases. Nat Rev Mol Cell Biol 2012;13:297–311.
46. Thirman MJ, Gill HJ, Burnett RC, Mbangkollo D, McCabe NR, Kobayashi H, et al. Rearrangement of the MLL gene in acute lymphoblastic and acute myeloid leukemias with 11q23 chromosomal translocations. N Engl J Med 1993;329:909–14.
47. Krivtsov AV, Twomey D, Feng Z, Stubbs MC, Wang Y, Faber J, et al. Transformation from committed progenitor to leukaemia stem cell initiated by MLL–AF9. Nature 2006;442:818–22.
48. Meyer C, Burmeister T, Gröger D, Tsaur G, Fechina L, Renneville A, et al. The MLL recombinome of acute leukemias in 2017. Leukemia 2018;32:273–84.
49. Kühn MWM, Song E, Feng Z, Sinha A, Chen CW, Deshpande AJ, et al. Targeting chromatin regulators inhibits leukemogenic gene expression in NPM1 mutant leukemia. Cancer Discov 2016;6:1166–81.
50. Tiacci E, Spanhol-Rosseto A, Martelli MP, Pasqualucci L, Quentmeier H, Grossmann V, et al. The NPM1 wild-type OCI-AML2 and the NPM1-mutated OCI-AML3 cell lines carry DNMT3A mutations. Leukemia 2012;26:554–7.
51. Chen Y, Jones KL, Anastassiadis K, Kranz A, Stewart AF, Grembecka J, et al. Distinct pathways affected by menin versus MLL1/MLL2 in MLL-rearranged acute myeloid leukemia. Exp Hematol 2019;69:37–42.
52. Kumar AR, Li Q, Hudson WA, Chen W, Sam T, Yao Q, et al. A role for MEIS1 in MLL-fusion gene leukemia. Blood 2009;113:1756–8.
53. Scacheri PC, Davis S, Odom DT, Crawford GE, Perkins S, Halawi MJ, et al. Genome-wide analysis of menin binding provides insights into MEN1 tumorigenesis. PLoS Genet 2006;2:e51.
54. Cheng J, Blum R, Bowman C, Hu D, Shilatifard A, Shen S, et al. A role for H3K4 monomethylation in gene repression and partitioning of chromatin readers. Mol Cell 2014;53:979–92.
55. Morgan MAJ, Shilatifard A. Reevaluating the roles of histone-modifying enzymes and their associated chromatin modifications in transcriptional regulation. Nat Genet 2020;52:1271–81.
56. Jang Y, Broun A, Wang C, Park YK, Zhuang L, Lee JE, et al. H3.3K4M destabilizes enhancer H3K4 methyltransferases MLL3/MLL4 and impairs adipose tissue development. Nucleic Acids Res 2019;47:607–20.
57. La P, Schnepp RW, D Petersen C, C Silva A, Hua X. Tumor suppressor menin regulates expression of insulin-like growth factor binding protein 2. Endocrinology 2004;145:3443–50.
58. Oldfield AJ, Henriques T, Kumar D, Burkholder AB, Cinghu S, Paulet D, et al. NF-Y controls fidelity of transcription initiation at gene promoters through maintenance of the nucleosome-depleted region. Nat Commun 2019;10:3072.
59. Jenuwein T, Allis CD. Translating the histone code. Science 2001;293:1074–80.
60. Akhtar A, Becker PB. Activation of transcription through histone H4 acetylation by MOF, an acetyltransferase essential for dosage compensation in Drosophila. Mol Cell 2000;5:367–75.
61. Bone JR, Lavender J, Richman R, Palmer MJ, Turner BM, Kuroda MI. Acetylated histone H4 on the male X chromosome is associated with dosage compensation in Drosophila. Genes Dev 1994;8:96–104.
62. Smith ER, Pannuti A, Gu W, Steurnagel A, Cook RG, Allis CD, et al. The Drosophila MSL complex acetylates histone H4 at lysine 16, a chromatin modification linked to dosage compensation. Mol Cell Biol 2000;20:312–8.
63. Shogren-Knaak M, Ishii H, Sun JM, Pazin MJ, Davie JR, Peterson CL. Histone H4-K16 acetylation controls chromatin structure and protein interactions. Science 2006;311:844–7.
64. Taylor GCA, Eskeland R, Hekimoglu-Balkan B, Pradeepa MM, Bickmore WA. H4K16 acetylation marks active genes and enhancers

of embryonic stem cells, but does not alter chromatin compaction. Genome Res 2013;23:2053–65.
65. Chen EY, Tan CM, Kou Y, Duan Q, Wang Z, Meirelles GV, et al. Enrichr: interactive and collaborative HTML5 gene list enrichment analysis tool. BMC Bioinf 2013;14:128–14.
66. Kuleshov MV, Jones MR, Rouillard AD, Fernandez NF, Duan Q, Wang Z, et al. Enrichr: a comprehensive gene set enrichment analysis web server 2016 update. Nucleic Acids Res 2016;44:W90–7.
67. Subramanian A, Tamayo P, Mootha VK, Mukherjee S, Ebert BL, Gillette MA, et al. Gene set enrichment analysis: a knowledge-based approach for interpreting genome-wide expression profiles. Proc Natl Acad Sci U S A 2005;102:15545–50.
68. Fridman AL, Tainsky MA. Critical pathways in cellular senescence and immortalization revealed by gene expression profiling. Oncogene 2008;27:5975–87.
69. Ruscetti M, Leibold J, Bott MJ, Fennell M, Kulick A, Salgado NR, et al. NK cell-mediated cytotoxicity contributes to tumor control by a cytostatic drug combination. Science 2018;362:1416–22.
70. Dang W, Steffen KK, Perry R, Dorsey JA, Johnson FB, Shilatifard A, et al. Histone H4 lysine 16 acetylation regulates cellular lifespan. Nature 2009;459:802–7.
71. Faget DV, Ren Q, Stewart SA. Unmasking senescence: context-dependent effects of SASP in cancer. Nat Rev Cancer 2019;19:439–53.
72. Agger K, Cloos PAC, Christensen J, Pasini D, Rose S, Rappsilber J, et al. UTX and JMJD3 are histone H3K27 demethylases involved in HOX gene regulation and development. Nature 2007;449:731–4.
73. Lan F, Bayliss PE, Rinn JL, Whetstine JR, Wang JK, Chen S, et al. A histone H3 lysine 27 demethylase regulates animal posterior development. Nature 2007;449:689–94.
74. Lee MG, Villa R, Trojer P, Norman J, Yan KP, Reinberg D, et al. Demethylation of H3K27 regulates polycomb recruitment and H2A ubiquitination. Science 2007;318:447–50.
75. Hong S, Cho Y-W, Yu L-R, Yu H, Veenstra TD, Ge K. Identification of JmjC domain-containing UTX and JMJD3 as histone H3 lysine 27 demethylases. Proc Natl Acad Sci U S A 2007;104:18439–44.
76. Shi B, Li W, Song Y, Wang Z, Ju R, Ulman A, et al. UTX condensation underlies its tumour-suppressive activity. Nature 2021;597:726–31.
77. Cao R, Wang L, Wang H, Xia L, Erdjument-Bromage H, Tempst P, et al. Role of histone H3 lysine 27 methylation in Polycomb-group silencing. Science 2002;298:1039–43.
78. Kuilman T, Michaloglou C, Mooi WJ, Peeper DS. The essence of senescence. Genes Dev 2010;24:2463–79.
79. Tasdemir N, Banito A, Roe J-S, Alonso-Curbelo D, Camiolo M, Tschaharganeh DF, et al. BRD4 connects enhancer remodeling to senescence immune surveillance. Cancer Discov 2016;6:612–29.
80. Placke T, Faber K, Nonami A, Putwain SL, Salih HR, Heidel FH, et al. Requirement for CDK6 in MLL-rearranged acute myeloid leukemia. Blood 2014;124:13–23.
81. Wang JK, Tsai MC, Poulin G, Adler AS, Chen S, Liu H, et al. The histone demethylase UTX enables RB-dependent cell fate control. Genes Dev 2010;24:327–32.
82. Hirai H, Roussel MF, Kato JY, Ashmun RA, Sherr CJ. Novel INK4 proteins, p19 and p18, are specific inhibitors of the cyclin D-dependent kinases CDK4 and CDK6. Mol Cell Biol 1995;15:2672–81.
83. Fry DW, Harvey PJ, Keller PR, Elliott WL, Meade MA, Trachet E, et al. Specific inhibition of cyclin-dependent kinase 4/6 by PD 0332991 and associated antitumor activity in human tumor xenografts. Mol Cancer Ther 2004;3:1427–37.
84. Yang C, Li Z, Bhatt T, Dickler M, Giri D, Scaltriti M, et al. Acquired CDK6 amplification promotes breast cancer resistance to CDK4/6 inhibitors and loss of ER signaling and dependence. Oncogene 2017;36:2255–64.
85. Chen L, Ye HL, Zhang G, Yao WM, Chen XZ, Zhang FC, et al. Autophagy inhibition contributes to the synergistic interaction between EGCG and doxorubicin to kill the hepatoma Hep3B cells. PLoS One 2014;9:e85771.
86. Kempinska K, Malik B, Borkin D, Klossowski S, Shukla S, Miao H, et al. Pharmacologic inhibition of the Menin-MLL interaction leads to transcriptional repression of PEG10 and blocks hepatocellular carcinoma. Mol Cancer Ther 2018;17:26–38.
87. Klossowski S, Miao H, Kempinska K, Wu T, Purohit T, Kim E, et al. Menin inhibitor MI-3454 induces remission in MLL1-rearranged and NPM1-mutated models of leukemia. J Clin Invest 2020;130:981–97.
88. Qiu H, Jin BM, Wang ZF, Xu B, Zheng QF, Zhang L, et al. MEN1 deficiency leads to neuroendocrine differentiation of lung cancer and disrupts the DNA damage response. Nat Commun 2020;11:1009.
89. Karnik SK, Hughes CM, Gu X, Rozenblatt-Rosen O, McLean GW, Xiong Y, et al. Menin regulates pancreatic islet growth by promoting histone methylation and expression of genes encoding p27Kip1 and p18INK4c. Proc Natl Acad Sci U S A 2005;102:14659–64.
90. Schnepp RW, Mao H, Sykes SM, Zong WX, Silva A, La P, et al. Menin induces apoptosis in murine embryonic fibroblasts. J Biol Chem 2004;279:10685–91.
91. Jeong KW, Andreu-Vieyra C, You JS, Jones PA, Stallcup MR. Establishment of active chromatin structure at enhancer elements by mixed-lineage leukemia 1 to initiate estrogen-dependent gene expression. Nucleic Acids Res 2014;42:2245–56.
92. Xu J, Li L, Xiong J, denDekker A, Ye A, Karatas H, et al. MLL1 and MLL1 fusion proteins have distinct functions in regulating leukemic transcription program. Cell Discovery 2016;2:16008–11.
93. Aubrey BJ, Cutler JA, Bourgeois W, Donovan KA, Gu S, Hatton C, et al. IKAROS and MENIN coordinate therapeutically actionable leukemogenic gene expression in MLL-r acute myeloid leukemia. Nat Cancer 2022;3:595–613.
94. Dhar SS, Zhao D, Lin T, Gu B, Pal K, Wu SJ, et al. MLL4 is required to maintain broad H3K4me3 peaks and super-enhancers at tumor suppressor genes. Mol Cell 2018;70:825–41.
95. Chen B, Gilbert LA, Cimini BA, Schnitzbauer J, Zhang W, Li GW, et al. Dynamic imaging of genomic loci in living human cells by an optimized CRISPR/Cas system. Cell 2013;155:1479–91.
96. Akama-Garren EH, Joshi NS, Tammela T, Chang GP, Wagner BL, Lee DY, et al. A modular assembly platform for rapid generation of DNA constructs. Sci Rep 2016;6:16836–9.
97. Doench JG, Fusi N, Sullender M, Hegde M, Vaimberg EW, Donovan KF, et al. Optimized sgRNA design to maximize activity and minimize off-target effects of CRISPR-Cas9. Nat Biotechnol 2016;34:184–91.
98. Sanjana NE, Shalem O, Zhang F. Improved vectors and genome-wide libraries for CRISPR screening. Nat Methods 2014;11:783–4.
99. Phillips RE, Yang Y, Smith RC, Thompson BM, Yamasaki T, Soto-Feliciano YM, et al. Target identification reveals lanosterol synthase as a vulnerability in glioma. Proc Natl Acad Sci U S A 2019;116:7957–62.
100. Strezoska Ž, Licon A, Haimes J, Spayd KJ, Patel KM, Sullivan K, et al. Optimized PCR conditions and increased shRNA fold representation improve reproducibility of pooled shRNA screens. PLoS One 2012;7:e42341.
101. Li W, Xu H, Xiao T, Cong L, Love MI, Zhang F, et al. MAGeCK enables robust identification of essential genes from genome-scale CRISPR/Cas9 knockout screens. Genome Biol 2014;15:554.
102. Carroll TS, Liang Z, Salama R, Stark R, de Santiago I. Impact of artifact removal on ChIP quality metrics in ChIP-seq and ChIP-exo data. Front Genet. Frontiers; 2014;5:75.
103. Liao Y, Smyth GK, Shi W. The R package Rsubread is easier, faster, cheaper and better for alignment and quantification of RNA sequencing reads. Nucleic Acids Res 2019;47:e47.
104. Zhang Y, Liu T, Meyer CA, Eeckhoute J, Johnson DS, Bernstein BE, et al. Model-based analysis of ChIP-Seq (MACS). Genome Biol 2008;9:R137–9.
105. Nikolayeva O, Robinson MD. edgeR for differential RNA-seq and ChIP-seq analysis: an application to stem cell biology. Methods Mol Biol 2014;1150:45–79.
106. Yu G, Wang L-G, He Q-Y. ChIPseeker: an R/Bioconductor package for ChIP peak annotation, comparison and visualization. Bioinformatics 2015;31:2382–3.
107. Ramírez F, Dündar F, Diehl S, Grüning BA, Manke T. deepTools: a flexible platform for exploring deep-sequencing data. Nucleic Acids Res 2014;42:W187–91.

108. Shen L, Shao N, Liu X, NE ngs.plot: quick mining and visualization of next-generation sequencing data by integrating genomic databases. BMC Genomics 2014;15:284–14.
109. Zhu LJ, Gazin C, Lawson ND, Pagès H, Lin SM, Lapointe DS, et al. ChIPpeakAnno: a Bioconductor package to annotate ChIP-seq and ChIP-chip data. BMC Bioinformatics 2010;11:237.
110. Amemiya HM, Kundaje A, Boyle AP. The ENCODE blacklist: identification of problematic regions of the genome. Sci Rep. 2019;9:9354–5.
111. Love MI, Huber W, Anders S. Moderated estimation of fold change and dispersion for RNA-seq data with DESeq2. Genome Biol 2014;15:550.
112. Patro R, Duggal G, Love MI, Irizarry RA, Kingsford C. Salmon provides fast and bias-aware quantification of transcript expression. Nat Methods 2017;14:417–9.
113. Soneson C, Love MI, Robinson MD. Differential analyses for RNA-seq: transcript-level estimates improve gene-level inferences. F1000Res 2015;4:1521.